

ON THE LIMB DARKENING, SPECTRAL ENERGY DISTRIBUTION, AND TEMPERATURE STRUCTURE OF PROCYON

J. P. AUFDENBERG¹

National Optical Astronomy Observatory, 950 N. Cherry Ave, Tucson, AZ 85719, USA

H.-G. LUDWIG

Lund Observatory, Lund University, Box 43, 22100 Lund, Sweden

AND

P. KERVELLA

LESIA, UMR 8109, Observatoire de Paris-Meudon, 5 place Jules Janssen, 92195 Meudon Cedex, France

Draft version February 5, 2008

ABSTRACT

We have fit synthetic visibilities from 3-D (C0⁵BOLD + PHOENIX) and 1-D (PHOENIX, ATLAS 12) model stellar atmospheres of Procyon (F5 IV) to high-precision interferometric data from the VLTI Interferometer (K-band) and from the Mark III interferometer (500 nm and 800 nm). These data sets provide a test of theoretical wavelength dependent limb-darkening predictions. The work of Allende Prieto et al. has shown that the temperature structure from a spatially and temporally averaged 3-D hydrodynamical model produces significantly less limb darkening at 500 nm relative to the temperature structure of a 1-D MARCS model atmosphere with a standard mixing-length approximation for convection. Our direct fits to the interferometric data confirm this prediction. A 1-D ATLAS 12 model with “approximate overshooting” provides the required temperature gradient. We show, however, that 1-D models cannot reproduce the ultraviolet spectrophotometry below 160 nm with effective temperatures in the range constrained by the measured bolometric flux and angular diameter. We find that a good match to the full spectral energy distribution can be obtained with a composite model consisting of a weighted average of twelve 1-D model atmospheres based on the surface intensity distribution of a 3-D granulation simulation. We emphasize that 1-D models with overshooting may realistically represent the mean temperature structure of F-type stars like Procyon, but the same models will predict redder colors than observed because they lack the multicomponent temperature distribution expected for the surfaces of these stars.

Subject headings: convection — methods: numerical — stars: atmospheres — stars: fundamental parameters (colors, temperatures) — stars: individual (Procyon) — techniques: interferometric

1. INTRODUCTION

The connection between the transport of energy in stellar atmospheres and the limb darkening of stellar photospheres has been under investigation for nearly 100 years in the case of the Sun. Since 1906 (Schwarzschild 1966), the darkening of the solar limb has been investigated to understand the roles of convection and radiation in the transport of energy through the Sun’s atmosphere. Assuming that the mass absorption coefficient of the solar atmosphere was both wavelength and depth independent and that the angle-dependent intensity could be replaced by the mean intensity at each depth, Schwarzschild derived a center-to-limb intensity variation based on a purely radiative equilibrium temperature structure

$$\frac{I(\tau = 0, \cos \theta)}{I(0, 1)} = 1 - \beta(1 - \cos \theta) \quad (\beta = 2/3), \quad (1)$$

where τ is the optical depth, θ is the angle between the line-of-sight and the emergent intensity, and β is the linear limb-darkening (LD) coefficient. Schwarzschild showed this LD law to be more consistent with contem-

porary observations than a LD law based on an adiabatic equilibrium temperature structure. Milne (1921) improved on Schwarzschild’s mean intensity approximation and found that a radiative equilibrium temperature structure with improved flux conservation yielded a LD coefficient of $\beta = 3/5$ in better agreement with observations.

The studies of Schwarzschild and Milne were completed before hydrogen was recognized as the principal constituent of the Sun’s atmosphere by Payne (1925), before the work of Unsöld (1930) concerning the effects of hydrogen ionization on the stability of radiative equilibrium against convection, and before the importance of the bound-free and free-free opacity of the negative ion of hydrogen was recognized by Wildt (1939). Plaskett (1936) inverted solar LD observations to find a temperature structure inconsistent with radiative equilibrium, suggesting convection has a significant effect on limb darkening. Keenan (1938) showed that this conclusion was acceptable only if the adiabatic gradient began at optical depths considerably less than $\bar{\tau} \sim 2$, contrary to Unsöld’s calculations. The reasoning was that convection currents should transport little energy above the zone of instability and that radiative equilibrium should

¹ Michelson Postdoctoral Fellow

prevail at smaller optical depths significant to limb darkening. Plaskett's conclusion was further critiqued by Woolley (1941) who showed that it necessitates convective velocities large enough to blur the Fraunhofer lines. Woolley attributed the differences between the observations and the radiative equilibrium models to the frequency dependent opacity of the solar atmosphere, not yet included in the models. As model atmospheres were improved with the incorporation of line blanketing and mixing-length convection, subsequent studies (Münch 1945; Swihart 1956; Spiegel 1963; Travis & Matsushima 1973; Vernazza et al. 1976; Koutchmy et al. 1977) generally confirmed Woolley's suggestion and concluded that the effects of convection on limb darkening were subtle or insignificant. Recently, Castelli et al. (1997) have shown that an "approximate overshooting" modification to the standard one-dimensional (1-D) mixing-length convection treatment enhances convective transport at smaller optical depths and provides a better fit to solar LD observations than models without overshooting. Overshooting refers to the depth of convective penetration into layers of the atmosphere stable against convection under the Schwarzschild criterion.

Photospheric convection and limb darkening are again the focus of some of the most exciting observational and theoretical studies in astrophysics. Recently, space based photometric observations (Matthews et al. 2004) have put an upper limit on pressure mode oscillations excited by turbulent convection in the atmosphere of the F-subgiant Procyon. Precise ground based photometric microlensing observations are providing multi-band limb-darkening measurements of solar-like stars (Abe et al. 2003) and recent observations of this kind are challenging model LD predictions for cool giants (Fields et al. 2003). Increasingly precise long baseline interferometric measurements at optical and near infrared wavelengths (Wittkowski et al. 2004; Ohishi et al. 2004; Perrin et al. 2004) are providing new tests of LD predictions. Tests of these predictions are important because they aid not only in the interpretation of interferometric data, but in the studies of eclipsing binaries, transiting extrasolar planets and their host stars.

Along with these recent observational developments, 3-D, time dependent radiation hydrodynamical simulations (Stein & Nordlund 1998; Robinson et al. 2003) have been produced to study solar granulation. With the aid of such models, the study of spectral line formation in solar granulation (Asplund et al. 2004) has recently significantly revised the solar elemental oxygen abundance. These simulations model in great detail the transition from convection dominated transport to radiation dominated transport near the surface of the solar atmosphere. Self-consistent, and not employing the usual 1-D mixing-length theory, these simulations predict a spatially and temporally averaged temperature profile for the solar atmosphere which samples upflows and downdrafts across the model solar surface. Similar models have also been developed for cooler and more evolved stars (e.g., Freytag et al. 2002; Ludwig et al. 2002; Robinson et al. 2004). For the Sun, multi-wavelength LD observations are used to test the *intensities* predicted by these models in addition to spectroscopic tests of the *flux* predictions. Qualitatively, multiwavelength solar LD predictions from 3-D models (Asplund et al. 1999, fig. 3) and

1-D models with overshooting (Castelli et al. 1997, fig. 4) are in reasonable agreement with the observations of Neckel & Labs (1994). Both these studies find that standard 1-D mixing-length theory predicts limb darkening which is too strong, most noticeably in the blue (500 nm). A similar relationship between 3-D and 1-D limb-darkening predictions has been established for Procyon (Allende Prieto et al. 2002, hereafter, AP02). These predictions for Procyon have until now not been directly tested by long baseline interferometric observations and this is the principal motivation for this paper.

Procyon (α CMi, HR 2943, HD 61421), an F-type subgiant (F5 IV-V, Gray et al. 2001) with a white dwarf companion, has been a prime target for both observational and theoretical asteroseismological studies (Martić et al. 1999; Chaboyer et al. 1999) because its visual orbital solution and measured angular diameter provide well-constrained estimates of its fundamental stellar parameters: effective temperature, gravity, radius, and mass; most recently improved upon by Girard et al. (2000) and Kervella et al. (2004b). The model of AP02 reproduces spectral line shifts, signatures of convective motion, measured from very high resolution ($R \simeq 200,000$) spectroscopy of Procyon. A comparison between this 3-D model and a homogeneous, hydrostatic 1-D model atmosphere from the MARCS code (Asplund et al. 1997; Gustafsson et al. 1975), with mixing-length convection and the same effective temperature and gravity, shows that at $1 \mu\text{m}$ the normalized center-to-limb predictions are quite comparable, while at 450 nm the 1-D intensity profile is up to 20% fainter than the 3-D intensity profile at intermediate limb angles. This LD contrast can be quantified with respect to interferometric observations by comparing the predicted LD corrections for the two models. The LD correction is a model dependent scale factor between the angular size derived from the visibility data assuming a uniformly bright stellar disk and the true wavelength independent angular size corresponding to a physical radius (see e.g., Davis et al. 2000). From AP02, the monochromatic LD corrections at 450 nm are 1.081 (1-D model) and 1.064 (3-D model), a difference of 1.6%. In this paper we test this prediction by comparing both 1-D and 3-D models directly with precise interferometric visibility measurements obtained in two intermediate bands at 500 nm and 800 nm, and in the K-band at $2.2 \mu\text{m}$.

It is also interesting to compare the uncertainty in a typical interferometric effective temperature estimate ($\simeq 100\text{--}200$ K) with the horizontal temperature variation expected from 3-D models. The AP02 3-D model for Procyon shows a R.M.S spatial temperature variation of ~ 500 K (8%) at a depth defined by a Rosseland optical depth of unity. As a result, while the bolometric flux and the angular diameter provide a temperature which represents the bolometric output of the photosphere, a 1-D atmosphere with this temperature is not expected to accurately represent the spectral energy distribution. For this reason, in addition to testing the 3-D model limb-darkening predictions, we also compare predictions of a 3-D model atmosphere to archival spectrophotometry and Strömgren photometry.

The broad wavelength coverage needed for the interferometric test requires data from more than one interferometer. We use 500 nm and 800 nm data from

the Mark III interferometer (Shao et al. 1988) and 2.2 μm data from the Very Large Telescope Interferometer (VLTI), specifically its commissioning instrument VINCI (Kervella et al. 2004a). In §2 we describe the observations and present the observational data and in §3 we describe the model atmospheres and the computation of the synthetic visibilities and the synthetic spectrophotometry. In §4 we show the comparison of the synthetic visibilities computed from the model atmospheres with the visibility data and archival photometric data. These results are discussed in §5 and briefly summarized in §6.

2. OBSERVATIONS AND FUNDAMENTAL PARAMETERS

2.1. Interferometric Observations

2.1.1. VLTI Observations

The European Southern Observatory's Very Large Telescope Interferometer (Glindemann et al. 2003) has been operated on top of the Cerro Paranal, in northern Chile since March 2001. The new observations presented in this paper were obtained by combining coherently the light coming from the two VLTI test siderostats (0.35 m aperture) on the E0-G1 baseline of the VLTI (66 m in ground length).

We used the VINCI beam combiner (Kervella et al. 2003a) equipped with a regular K band filter ($\lambda = 2.0 - 2.4 \mu\text{m}$). While the observations presented by Kervella et al. (2004b) were limited to a maximum baseline of 24 m, the 22 new squared visibility measurements cover the 42–66 m range, significantly lower in the first lobe of the Procyon visibility curve. Both the 24 m and 66 m baseline data are listed in Table 1.

The raw data were processed using a wavelet based algorithm (Kervella et al. 2004a) to obtain the instrumental squared moduli of the coherence factors. The instrumental transfer function was deduced from observations of four calibrator stars (HR 1799, 6 Leo, 18 Mon and 30 Gem) whose *a priori* angular diameters were taken from the Cohen et al. (1999) list. Their linear limb darkening coefficients were taken from Claret (2000) tables for the K band. The 24 m baseline data previously published in Kervella et al. (2004b), as well as three points from the 66 m baseline, were calibrated using Sirius as the reference star. Its well-determined angular diameter (Kervella et al. 2003b) results in a small systematic uncertainty on the calibrated visibilities of Procyon. Furthermore, the Sirius-calibrated visibilities obtained on the longer E0-G1 baseline show no detectable deviation from the other calibrators. The other calibrators have small angular diameters compared to Procyon ($\approx 2 \text{ mas}$ vs. more than 5 mas). This translates into small systematic errors on the calibrated visibility data. These errors were carried through the data reduction process and are reported in Table 1, together with the associated calibrator stars.

Apart from Sirius, the calibrators of the VLTI-VINCI data are all K giants from the list established by Cohen et al. (1999). For this homogeneous set of stars, the limb darkening correction LD/UD is always in the 1.02–1.03 range. The LD correction for Procyon in the K band being just below LD/UD=1.02, it is almost identical and this correction cancels out. For Sirius, the effective temperature is higher ($\sim 10000 \text{ K}$), resulting in a smaller LD correction of 1.012. In order to take into

account properly this 0.7% difference, we have used the linear LD correction from Claret (2000). Considering the small amplitude of this correction (1.2%), the introduced systematic uncertainty is considered negligible compared to the VINCI error bar on the best estimate LD angular diameter of Procyon, $5.404 \pm 0.031 \text{ mas}$, $\pm 0.6\%$ (see §4). The infrared K band is an advantage in this matter, as the LD corrections are small, and do not change much over a broad range of effective temperatures.

2.1.2. Mark III Observations

The Mark III interferometric data presented here comprise visibility measurements at 800 nm (Mozurkewich et al. 1991, fig. 1(i)) from which uniform disk angular diameter fits have already been published (Mozurkewich et al. 1991, 2003) and unpublished visibility measurements at 500 nm from D. Mozurkewich (2004, private communication). We list these data in Tables 2 and 3 so that others may fit models directly to these visibilities. Mozurkewich et al. (1991, 2003) do not provide a listing of calibrator stars. They note, however, that the calibrator stars are all smaller than the program stars and we expect the calibrator visibilities to be largely insensitive to model-dependent systematic uncertainties due to limb darkening. Seriously large systematic errors seem to be ruled out by a comparison of the published Mark III uniform disk fits at 450 nm to the earlier Intensity Interferometer uniform disk fits at 443 nm (Hanbury Brown et al. 1974), which agree within 1σ .

2.2. Initial Fundamental Parameters

2.2.1. Effective Temperature

Fundamental stellar parameters for Procyon are well constrained by direct measures of its bolometric flux and angular diameter. The bolometric flux is derived from an integration of Procyon's spectral energy distribution (SED). Absolute spectrophotometry in the ultraviolet come from the *International Ultraviolet Explorer* (low dispersion, large aperture spectra SWP43428 and LWR09108 from the INES archive (Rodríguez-Pascual et al. 1999), effectively from 170 nm to 306 nm), and from the *Hubble Space Telescope* Space Telescope Imaging Spectrograph (10 one-dimensional extracted spectra in the sequence 06l501020 to 06l5010k0 from 220 nm to 410 nm). For integration, the ultraviolet data are binned to 1 nm resolution. Absolute spectrophotometry in the visual and near-infrared wavelength range (322.5 nm – 1027.5 nm, 5 nm resolution) has been obtained by Glushneva et al. (1992). For the SED beyond 1 micron, the broad-band photometry (JHKLMN) from Morel & Magnenat (1978), with the absolute calibration of Johnson (1965) for JKLMN and Bessell & Brett (1988) for H, is fit using linear interpolation in $\log \lambda - \log F_\lambda$ space. We have adopted a uniform flux uncertainty of 5% for all the spectrophotometric data. The most carefully calibrated photometric standards are not likely to be more accurate than 4% in the absolute sense (Bohlin & Gilliland 2004). On the basis of Procyon's distance (3.5 pc), interstellar dust extinction is assumed to be negligible. The integrated flux from 170 nm to 10200 nm is $17.82 \pm 0.89 \times 10^{-9} \text{ W m}^{-2}$. This value is in good agreement with the value

$18.08 \pm 0.76 \text{ W m}^{-2}$ derived by Code et al. (1976). The difference in the integrated flux between STIS and *IUE* over their common wavelength range is less than 1%. The integrated STIS flux is $\sim 6\%$ larger than the integrated Glushneva et al. (1992) flux between 322 nm and 410 nm. Our integrated flux and the limb-darkened angular diameter ($\theta_{\text{LD}} = 5.45 \pm 0.05 \text{ mas}$) from Kervella et al. (2004b) yield $T_{\text{eff}} = 6516 \pm 87 \text{ K}$. This value is in good agreement with $T_{\text{eff}} = 6510 \pm 150 \text{ K}$ from Code et al. (1976). A comparison of the angular diameter uncertainty (0.9%) and the integrated flux uncertainty (5%) shows that the uncertainty in T_{eff} is dominated by the uncertainty in the spectrophotometry.

2.2.2. Radius and Surface Gravity

The *HIPPARCOS* parallax ($285.93 \pm 0.88 \text{ mas}$, Perryman et al. 1997) and the angular diameter ($\theta_{\text{LD}} = 5.45 \pm 0.05 \text{ mas}$) yield a radius of $2.05 \pm 0.02 R_{\odot}$. The orbital solution of Girard et al. (2000) provides a mass for Procyon A, which is $1.42 \pm 0.04 M_{\odot}$ adopting the *HIPPARCOS* parallax (Kervella et al. 2004b). The mass together with the radius yields a surface gravity, $\log(g) = 3.95 \pm 0.02$ (in cgs units), which is uncertain at the 5% level.

3. MODEL ATMOSPHERES

The construction of model atmospheres for Procyon and the subsequent calculation of synthetic radiation fields for comparison with interferometry and photometry is done three ways: (1) Stand-alone 1-D PHOENIX (Hauschildt et al. 1999) structures, radiation fields and spectra ; (2) CO^5BOLD (Freytag et al. 2002) 3-D structures temporally and spatially averaged to 1-D, then read by PHOENIX for computation of the corresponding radiation fields; (3) Stand-alone 1-D ATLAS 12 (Kurucz 1992) structures, radiations fields and spectra. These models will be discussed in more detail below.

3.1. Input Parameters

The ATLAS 12 models are plane parallel and require an effective temperature T_{eff} and a surface gravity, $\log(g)$, as input parameters. The spherical PHOENIX models additionally require a stellar radius because in the spherical case the luminosity, not the flux, is constant. For Procyon's photosphere this distinction is negligible, however the boundary radii of the spherical and plane-parallel models differ as discussed below. CO^5BOLD models a local, 3-D, statistically representative volume of the stellar atmosphere in Cartesian geometry with periodic lateral boundaries. As input parameters CO^5BOLD requires the surface gravity and the specific entropy of material entering the computational volume through the open lower boundary. The entropy strongly influences the amount of heat entering the volume from below, and plays a role analogous to the effective temperature in the 1-D models.

3.2. PHOENIX Models

A grid of forty-two 1-D, spherical, hydrostatic models from the PHOENIX general-purpose stellar and planetary atmosphere code (version 13.07, for a description see Hauschildt et al. 1999; Hauschildt & Baron 1999) have been constructed with the following parameters: effective temperatures, $T_{\text{eff}} = 6420 \text{ K}$ to 6620 K , 10 K steps;

$\log(g) = 3.95$, radius, $R = 1.46 \times 10^{11} \text{ cm}$; depth-independent micro-turbulence, $\xi = 2.0 \text{ km s}^{-1}$ (a value suggested for 1-D models by AP02 from their analysis of Procyon's spectrum); mixing-length to pressure scale ratio, $\alpha = 0.5$ and 1.25 ; solar elemental abundance (Anders & Grevesse 1989); LTE atomic and molecular line blanketing, typically 10^6 atomic lines and 4×10^5 molecular lines dynamically selected at run time; non-LTE line blanketing of H I (30 levels, 435 bound-bound transitions), He I (19 levels, 171 bound-bound transitions), and He II (10 levels, 45 bound-bound transitions); and boundary conditions: outer pressure, $P_{\text{gas}} = 10^{-4} \text{ dynes cm}^{-2}$, extinction optical depth at $1.2 \mu\text{m}$: outer 10^{-10} , inner 10^2 . For this grid of models the atmospheric structure is computed at 100 radial shells (depths) and the radiative transfer is computed along 100 rays tangent to these shells and 14 additional rays which impact the innermost shell, the so-called core-intersecting rays. The intersection of the rays with the outermost radial shell describes a center-to-limb intensity profile with 114 angular points. The mixing-length theory for convection in PHOENIX is very similar to the Mihalas formulation (Ludwig et al. 2002; Mihalas 1978) with no overshooting. A second grid of 24 PHOENIX models has been constructed as components to composite models which simulate the effects of granulation on the spectral energy distribution (see §3.6, Table 4). Other than T_{eff} , these models have the same input parameters as the first grid. The non-LTE H and He aspect the stand-alone PHOENIX models is an insignificant factor for the angular diameter fits and synthetic spectrophotometry presented here, as we have confirmed by converging purely LTE PHOENIX models for comparison. The H^- ion is treated in LTE for all the PHOENIX models. The effects of treating many thousands of lines out of LTE in a solar-type star has been recently explored by Short & Hauschildt (2005). Such effects could be important for the synthetic spectrophotometry, however such massive-scale non-LTE models for Procyon have yet to be calculated and are beyond the scope of this paper. Below we specifically refer to PHOENIX models "A" and "B". For both models $T_{\text{eff}} = 6530 \text{ K}$ and $\log(g) = 3.95$ (consistent with the values derived in §2.2), but they have different values for α , 1.25 and 0.5, respectively.

3.3. CO^5BOLD and PHOENIX Models

The "CONservative COde for COmputation of COmpressible COnvection in a BOx of L Dimensions ($L = 2, 3$)" (CO^5BOLD) was mainly developed by B. Freytag and M. Steffen (for details see Freytag et al. 2002; Wedemeyer et al. 2004). The CO^5BOLD models (series codes d3gt65g40n2.80-a4-3 (grey) and d3gt65g40n3.10-26-3 (non-grey)) for Procyon have an average $T_{\text{eff}} = 6500 \text{ K}$, a prescribed $\log(g) = 4.0$, and solar abundances. For the non-grey model, five wavelength groups are employed to describe the wavelength dependence of the radiation field within a multi-group radiative transfer scheme (Ludwig 1992). The group-averaged opacities are based on data provided by the ATLAS 6 code (Kurucz 1979).

Integration with the 1-D PHOENIX code provides direct opacity sampling at high spectral resolution for calculation of the radiation field based temperature structures provided by CO^5BOLD . The 1-D temperature, pressure, and depth arrays (91 depth points) from CO^5BOLD

are read by **PHOENIX**. The physical depths provided by **CO⁵BOLD** are relative to the layer where the average Rosseland optical depth is unity, but **PHOENIX** requires absolute radii for construction of the 1-D spherical radiation field. The value 1.46×10^{11} cm, corresponding to the physical radius of Procyon, is therefore added to the **CO⁵BOLD** depths. The accuracy of this value is not critical because the thickness of the atmosphere is $\sim 0.1\%$ of the stellar radius.

We take two approaches for the computation of the mean radiation field of the **CO⁵BOLD** models. (1) we compute a **PHOENIX** radiation field from a temporally and spatially averaged 3-D temperature structure. (2) we compute 980,000 horizontal positions from the spatial and temporal evolution of the granular flow (see Figure 1 for a snapshot of the flow) and sort them into 12 groups according to their intensity (see Figure 2 for the histogram of intensities). Next, we average the vertical slabs on surfaces of fixed optical depth. This results in twelve temperature stratifications representing the dark and increasingly brighter granulation areas. **PHOENIX** radiation fields are then computed for each of the twelve structures. These radiation fields are then co-added, weighted by the surface areas of the twelve intensity groups (for weights see Table 4). Theoretically, we expect approach (2) provides a better match to the actual radiation field of Procyon. This is because radiative transfer in an inhomogeneous medium is non-linear and one cannot interchange radiative transfer and spatial averaging exactly. In this respect, the twelve component model should be an improvement over a global spatial mean.

We find the temporally and spatially averaged temperature structures from the grey and non-grey **CO⁵BOLD** models are nearly identical at the depths of continuum formation for the interferometric wavebands considered here: 500 nm, 800 nm, and 2.2 μm . As a result, the corresponding **PHOENIX** radiation fields from approach (1) yield fit angular diameters that differ by less than 0.03%. Much greater than the grey versus non-grey effects are the differences using approaches (1) and (2). Using the weighted average of the twelve radiation fields to simulate the mean center-to-limb profile yields an angular diameter 0.4% larger at 500 nm compared to the global spatial mean radiation field. As we show in §4, approach (2) is slightly more consistent with the observed visibility data. Below we refer to models “C1” and “C2”, models constructed via approaches (1) and (2), respectively.

Tests indicate that the **PHOENIX** radiation field produced from the **CO⁵BOLD** 1-D average structure produces an outer boundary radiative flux lower than expected (by 15% in flux, 260 K in T_{eff}) for an effective temperature of 6500 K. This is most likely due to the different opacity setups in the two codes. **CO⁵BOLD** uses the older **ATLAS 6** opacity setup. As a result, a spectral energy distribution from **PHOENIX** based on the mean 3-D structure will be cooler than expected from the **CO⁵BOLD** T_{eff} value. This is not a critical problem for the interferometric comparisons because of the insensitivity of the limb-darkening to T_{eff} in this range (5500 K to 7500 K, see §5.2). The radiative flux mismatch is a problem with regards to synthetic photometry and this is discussed below in §3.6.

3.4. ATLAS 12 Models

We also use **ATLAS 12** models (Kurucz 1992, and R. L. Kurucz 2004, private communication) which include an “approximate overshooting” (AO) prescription for convective flux transport in a mixing-length formalism (Castelli et al. 1997, sec. 2.3), for comparison with the 1-D and 3-D models just discussed. In the AO formulation, the convective flux extends to lower optical depths, reducing the temperature gradient relative to models without overshooting. Three **ATLAS 12** models have been constructed: “D”, no overshooting; “F”, 50% overshooting; and “E” full overshooting. All three models have the following parameters: $T_{\text{eff}} = 6530$ K; $\log(g) = 3.95$; the microturbulence is depth dependent increasing from 0.9 km s^{-1} to 3.2 km s^{-1} at the inner boundary; $\alpha = 1.25$; solar elemental abundance (Anders & Grevesse 1989); LTE atomic and molecular line blanketing; and boundary conditions: outer $\tau_{\text{Ross}} = 10^{-7}$, inner $\tau_{\text{Ross}} = 10^2$. After the models, with 72 depth points, were computed by opacity sampling, the complete spectrum was computed at resolving power of $R=500,000$ for 17 angular “ μ ” points describing the center-to-limb intensity profile.

3.5. Synthetic Visibilities and Fit Procedure

The computation of the synthetic visibilities from the model radiation fields simulates the bandwidth-smeared squared visibility (see e.g., Davis et al. 2000). At a projected baseline B and mean wavenumber λ_0^{-1} , the synthetic squared visibility,

$$V(B, \lambda_0)^2 = \frac{\int_0^\infty V(B, \lambda)^2 \lambda^2 d\lambda}{\int_0^\infty S(\lambda)^2 F_\lambda^2 \lambda^2 d\lambda}, \quad (2)$$

is computed at each wavelength from a Hankel transform,

$$V(B, \lambda) = \int_0^1 S(\lambda) I(\mu, \lambda) J_0 \left[\pi \theta_{\text{LD}}(B/\lambda) (1-\mu^2)^{1/2} \right] \mu d\mu, \quad (3)$$

where $I(\mu, \lambda)$ is the model radiation field (in photons $\text{cm}^{-2} \text{s}^{-1} \text{sr}^{-1}$), $S(\lambda)$ is the instrument sensitivity curve, μ is the cosine of the angle between the line of sight and the surface normal, and θ_{LD} is the limb-darkened angular size. The mean wavenumber is computed from

$$\lambda_0^{-1} = \frac{\int_0^\infty \lambda^{-1} S(\lambda) F_\lambda d\lambda}{\int_0^\infty S(\lambda) F_\lambda d\lambda}, \quad (4)$$

where

$$F_\lambda = 2\pi \int_0^1 I(\mu, \lambda) \mu d\mu \quad (5)$$

is the flux. For each model radiation field, non-linear least squares fits are performed to the visibility data at 500 nm, 800 nm, and 2.2 μm , using the Interactive Data Language (IDL) routine **CURVEFIT**, yielding three values for θ_{LD} .

The baselines for the **VINCI** visibilities are listed in Table 1. The reciprocal of the mean wavenumber for the **VINCI** transmission (including: K-band filter, detector quantum efficiency, fibers, atmosphere, and MONA beam combiner) is $\lambda_0 = 2.182 \pm 0.002 \mu\text{m}$ using an appropriate synthetic spectrum for Procyon (a $T_{\text{eff}}=6530$ K, $\log(g) = 3.95$ **PHOENIX** model). An accurate estimate for the mean wavenumber is important because the fit angular diameter scales linearly with the mean wavenumber.

The Mark III sensitivity curves are assumed to be Gaussian with central wavelengths $\lambda_0 = 500$ nm and 800 nm, each with a FWHM of 20 nm (Mozurkewich et al. 1991). The Mark III bands are ~ 20 times narrower than the VINCI band, therefore the mean wavenumber is much less sensitive to the shape of Procyon's spectral energy distribution.

3.5.1. Accounting for Extension in the Spherical Models

A proper comparison of the best fit θ_{LD} values derived from PHOENIX, CO⁵BOLD +PHOENIX, and ATLAS 12 models requires a correction to the stand-alone PHOENIX values because of spherical extension effects. The PHOENIX structures extend outward to a radial shell $\simeq 0.4\%$ above the $\tau_{\text{ross}} = 1$ radius while the model plane-parallel structures have very small extensions for a fixed gravity (the CO⁵BOLD and ATLAS 12 structures have extensions of $\simeq 0.1\%$). The radiation field $I(\mu, \lambda)$ refers to the angular distribution of intensities emerging from the outermost model layer. As a result, the spherical models with greater radial extension yield larger angular sizes relative to the less extended plane-parallel models. This is true even when the angular size of the continuum-forming radii for the two model geometries agree because their outer boundary radii differ. Thus, the PHOENIX θ_{LD} values have been scaled down to correspond with the $\tau_{\text{ross}} = 1$ radius (in other words reduced by 0.4%) for comparison with the plane-parallel models. For red giants the correction is much larger, for example 7% in the case of ψ Phe (Wittkowski et al. 2004). This correction reminds us that even relatively compact atmospheres are “fuzzy” and that the stellar radius must be carefully defined (Baschek et al. 1991). The need for this correction also speaks to the precision of the observational data.

3.6. Synthetic Spectrophotometry and Photometry with 3-D and 1-D Models

At present, the coarseness of the wavelength-dependent opacity in the CO⁵BOLD model does not permit direct predictions of accurate colors. Therefore, we use the spatial intensity distribution of the 3-D model as a guide to construct multicomponent models of Procyon's granulation pattern with PHOENIX. From the grey CO⁵BOLD model a snapshot of the emergent intensity in integrated (“white”) light is shown in Figure 1, Figure 2 depicts a histogram of intensities, including 12 intensity intervals for which we construct PHOENIX models (see Table 4 for corresponding surface area weights). The bimodal nature of the histogram shows that the model photosphere can be divided roughly into “cool” and “hot” components, as also indicated in the intensity map. In fact, we initially experimented with such a two-component model, and later refined the spectral synthesis to the present 12-component model.

For constructing the PHOENIX models we need to specify a T_{eff} . Assuming a linear darkening law

$$\frac{I_{\lambda}(\mu)}{I_{\lambda}(1)} = 1 - \beta(1 - \mu) \quad (6)$$

we convert emergent intensities in vertical direction to fluxes F according to

$$F_{\lambda} = \pi I_{\lambda}(1) \left(1 - \frac{\beta}{3}\right). \quad (7)$$

With the additional assumption of a wavelength independent β we directly obtain T_{eff} since the grey CO⁵BOLD model provides wavelength integrated intensities. The T_{eff} of the inner 10 zones are taken as the average of the T_{eff} at the two adjacent boundaries. For the two outer zones half the interval width ΔT_{eff} of the adjacent zone is added (subtracted) to the hottest (coolest) boundary. The radiation fields of the individual components are added, weighted by the surface area fraction associated with the represented intensity interval. The resulting T_{eff} values and weights for the 12 zones are listed in Table 4. Two values for β have been chosen: 0.5 and 0.6. These values are consistent with published linear limb-darkening coefficients for broad-band optical filters (Claret 2000). More importantly, these two β values yield T_{eff} distributions which, after the twelve 1-D model SEDs are weighted and co-added, have bolometric fluxes and corresponding effective temperatures which bracket the CO⁵BOLD model ($T_{\text{eff}} = 6500$ K). The composite spectrum T_{eff} is computed as

$$T_{\text{eff}} = \left\{ \frac{1}{\sigma} \int_0^{\infty} \left[\sum_{i=1}^{i=12} w^i F_{\lambda}^i \right] d\lambda \right\}^{1/4} \quad (8)$$

where σ is the Stefan-Boltzmann constant, w^i are the weights given in Table 4, and F_{λ}^i are the flux distributions from the component models.

3.6.1. Synthetic Photometry

Synthetic Strömgren indices (Strömgren 1966) are computed using the formulae of Matsushima (1969). In this formalism, a normalization constant, or zero point, k_{ij} is needed to transform each natural index,

$$(i - j)_{\text{nat}} = 2.5 \log \left\{ \frac{\int_0^{\infty} F_{\lambda} S_j(\lambda) d\lambda}{\int_0^{\infty} F_{\lambda} S_i(\lambda) d\lambda} \right\} \quad (9)$$

to a photometric index,

$$(i - j) = (i - j)_{\text{nat}} + k_{ij} \quad (10)$$

directly comparable to observations. In the literature, the normalization of the theoretical indices is often based solely on models of Vega (e.g., Smalley & Kupka 1997), however Lester et al. (1986) have shown that these zero points are a function of $(b - y)$. Since Vega and Procyon do not have the same $(b - y)$, using Vega leads to systematic errors in the synthetic indices. We also wish for obvious reasons not to use a model of Procyon to obtain these zero points. Therefore, we use two independent spectrophotometric observations of Procyon (Kiehling 1987; Glushneva et al. 1992) and two different sets of filter sensitivity curves (Matsushima 1969; Crawford & Barnes 1970) to determine the following zero points:

$$(b - y)_{\text{obs}} - (b - y)_{\text{nat}} = +0.503 \pm 0.004 \pm 0.007 \quad (11)$$

$$(c_1)_{\text{obs}} - (c_1)_{\text{nat}} = -0.088 \pm 0.003 \pm 0.009 \quad (12)$$

These zero points are given with two sets of uncertainties. The first set arises from the range of zero points obtained using the four different filter/spectrophotometric data combinations. The second

set is from to the mean observational error in the observed indices (Crawford & Barnes 1970). If we use spectrophotometry of Vega (Bohlin 1996) the mean c_1 zero point is instead -0.165 mag, consistent with the c_1 shift shown by Lester et al. (1986) at the $(b - y)$ color (0.272) of Procyon.

4. RESULTS

4.1. Multiwavelength Angular Diameter Fits

Table 5 lists the best fit θ_{LD} values (and 1σ uncertainties) at 500 nm, 800 nm, and $2.2 \mu\text{m}$ for seven different atmospheric structures and a uniform disk model. Figure 3 shows all the visibility data together with the synthetic visibilities from the CO⁵BOLD + PHOENIX model “C2” with the mean fit angular diameter of 5.403 mas. The best fit angular diameters for all seven models are compared in Figure 4.

There is a clear trend in the fit results toward shorter wavelengths. The seven models yield a significantly wide range of angular diameters at 500 nm, differing by $100 \pm 23 \mu\text{as}$, while differing only by $17 \pm 12 \mu\text{as}$ at $2.2 \mu\text{m}$. Of the seven models, two models stand out as best representing the visibility data at all three wavelengths with a single angular diameter: CO⁵BOLD + PHOENIX model “C2” and ATLAS 12 model “F” (with 50% overshooting). Both models yield angular diameters at the 500 nm and $2.2 \mu\text{m}$ that are the same within the formal uncertainties: $15 \pm 17 \mu\text{as}$ and $4 \pm 17 \mu\text{as}$, respectively. Unlike model “F”, model “C2” has no free parameters for convection.

4.2. Model Comparisons to Spectrophotometry and Photometry

Figure 5(a) shows that the synthetic SED of ATLAS 12 model “E” fails to reproduce the observed continuum below 160 nm. This is true not only for model “E”, but all 1-D models, regardless of convection treatment, which are consistent with both the measured angular diameter and the measured bolometric flux. While the contribution to Procyon’s bolometric flux from radiation between 130 nm and 160 nm is negligible, the absolute flux level in this region provides strong evidence for a multicomponent temperature surface distribution and therefore granulation.

The absolute continuum fluxes between 136 nm and 160 nm are from the Goddard High Resolution Spectrograph data sets: Z2VS0105P (PI A. Boesgaard), Z17X020CT, Z17X020AT, Z17X0208T (PI J. Linsky). These spectra were originally obtained to study the Procyon’s atmospheric boron abundance (Cunha et al. 2000) and chromosphere (Wood et al. 1996). The signal-to-noise in the continua of these spectra ranges from approximately 4:1 in the bluest data set to 10:1 in the reddest data set. These data are far superior to any other measurements below 160 nm because the continuum drops by more than a factor of 100 here, too much for the limited dynamic range of *IUE*. The absolute fluxes below 160 nm shown in Figure 5 were estimated by computing the mean flux between the emission lines in each spectrum incorporating the flux uncertainties provided with each calibrated data set.

The observed continuum below 160 nm is consistent with a spatial component of Procyon’s atmosphere which has a color temperature in excess of the interferometric

T_{eff} . Therefore, such a component must represent a small fraction of the surface, for it would otherwise produce a bolometric flux in excess of that observed. The continuum of Procyon between 136 nm and 160 nm should be photospheric, in contrast to the solar spectrum where the bound-free opacity of silicon causes the continuum to form at or slightly above the temperature minimum, near the base of the chromosphere (Vernazza et al. 1976). Procyon’s overall warmer photosphere ($T_{\text{eff}} = 6540$ K vs. $T_{\text{eff}} = 5770$ K) will contribute more flux to this spectral region than does the Sun. Furthermore, the warmer components of Procyon’s photosphere, which predominately contribute to the continuum below 160 nm, have a silicon bound-free opacity approximately three times weaker than expected for solar photospheric conditions (Travis & Matsushima 1968, fig. 6). Thus we expect Procyon’s continuum between 136 nm and 160 nm to form at depths beneath its chromosphere.

The ultraviolet SED longward of 160 nm, where the multicomponent temperature effects are less prominent, may be impacted by non-LTE treatment of iron-group elements. Short & Hauschildt (2005) find non-LTE models for the Sun have substantially (up to 20%) more near-UV flux relative to LTE models. Whether such differences would exist for a similar non-LTE model of Procyon is not clear.

The lower panel of Figure 5 shows the ATLAS 12 model “E” SED matches the Composite SED B model fairly well in the *u*- and *y*-bands, but has significantly lower flux in the *b*- and *v*-bands. In the composite SED model the peaks of the 12 components all contribute flux to the *v*- and *b*-bands, while at longer wavelengths the flux contrast is lower. Table 6 and Figure 6 show that the $T_{\text{eff}} = 6530$ K ATLAS 12 models all predict $(b - y)$ values significantly redder than observed. In particular, the $(b - y)$ value for ATLAS 12 model “F”, the best fitting 1-D model to the interferometric data, differs by $+0.04$ mag, significantly in excess of the estimated uncertainties (0.012 mag, see §3.6.1).

The differences in the derived indices between PHOENIX model “A” and ATLAS 12 model “D”, particularly for c_1 , result from differences in these models’ temperature structures (see Figure 7). While these two 1-D models were constructed to have the same input parameters, they differ in geometry (spherical vs. plane parallel) and line formation (non-LTE versus LTE treatment of hydrogen and helium and constant vs. depth-dependent microturbulence) assumptions. To investigate this discrepancy, we converged two LTE, plane-parallel PHOENIX models with constant microturbulences of 0 and 2 km s^{-1} . These models yield colors nearly identical to model “A”, suggesting that the 1-D mixing-length convection treatments (without overshooting) differ between PHOENIX and ATLAS 12. A difference in the convection treatments of these two codes is noted by Short & Hauschildt (2005).

5. DISCUSSION

5.1. Model Differences, Interferometric Uncertainties, and Future Measurements

As predicted by AP02, we find, based on comparisons with high-precision multiwavelength interferometric data, that 1-D model temperature structures based on standard mixing-length theory (without overshoot-

ing) produce center-to-limb intensity profiles which are too limb darkened at blue wavelengths relative to near-IR wavelengths. The magnitude of this effect appears to be slightly smaller than predicted, 0.4 – 1.5% versus 1.6%, depending on which 1-D model is adopted. Furthermore, limb-darkening predictions from a 3-D hydrodynamical model appear to be consistent with these data, also in line with AP02’s predictions.

Considering the three **ATLAS 12** models, the fit angular diameters differ negligibly (0.2%) at 2.2 μm , but differ by 1.1% at 500 nm due to different convection treatments. Considering all seven model atmospheres, from **PHOENIX**, **ATLAS 12** and **C0⁵BOLD + PHOENIX**, the range of fit angular diameters is again small (0.3%) at 2.2 μm , with differences up to 1.9% at 500 nm. The error bars on the interferometric data sets yield formal uncertainties of 0.1% to 0.2% in the absolute angular diameters. It should therefore be possible to choose between these models in the absence of significant systematic errors. Any systematic errors in the VLTI/VINCI angular diameters is expected to be less than 0.3% (Kervella et al. 2004b). The systematic errors in the Mark III are not as well characterized, however the three 1-D models without overshooting yield larger angular diameters at 500 nm relative to 800 nm as expected, while the 3-D **C0⁵BOLD + PHOENIX** model “C2” and **ATLAS 12** model “F” for 50% overshooting yield the same angular diameters. These relationships hold out to 2.2 μm , where model “C2” yields the same angular diameter within 1.3σ . This suggests that systematic errors between the VLTI/VINCI and Mark III data sets are minimal.

Table 5 and Figure 4 show that an angular diameter derived from the VLTI/VINCI visibilities is the least sensitive to which model is employed. The mean angular diameter value at 2.2 μm together with 1σ range in angular diameters (0.26%) and the upper limit on the systematic error in the VLTI/VINCI diameter (0.3%) yields a best estimate for the angular diameter of Procyon: 5.404 ± 0.031 mas. The corresponding best estimates for T_{eff} , radius, and surface gravity are listed in Table 7.

Interferometric observations with superior calibration are certainly warranted to check these results. Independent multiwavelength angular diameter measurements are in order, however this is not the only approach presently available. Limb darkening, in addition to its affect on these angular diameter measurements, can be constrained by a precise measurement of the second lobe of the visibility curve. While angular diameters derived from the 3-D and standard 1-D models differ by only 1% at 500 nm, the squared visibility at the peak of the second lobe is predicted to differ by 10% at 500 nm. At longer wavelengths the predicted difference is smaller: 6% at 800 nm and 3% at 2.2 μm . Precise second lobe measurements at 500 nm and 800 nm could possibly be made with the Navy Prototype Optical Interferometer (NPOI) and the Sydney University Stellar Interferometer (SUSI). Distinguishing between the 3-D **C0⁵BOLD** model and 1-D overshooting **ATLAS 12** model “F” on the basis of second lobe measurements would appear to be much more challenging. The squared visibility amplitudes at the peak of the 2nd lobe for these two models differ by less than 1% at 500 nm, 800 nm, and 2.2 μm .

5.2. Procyon’s Mean Temperature Gradient

The continuum forming region of Procyon’s atmosphere is expected to have a physical thickness which is very small ($< 0.1\%$) in comparison with its stellar radius. Therefore, the wavelength-dependent uniform disk angular diameter is unlikely to result from an extended atmosphere where significantly different physical depths are probed at different wavelengths, as in the case of cool supergiants. Instead this effect must reside in the distribution of temperature with optical depth.

The best fit angular diameter values presented in Table 5 and Figure 4 are quite insensitive to the model effective temperature. Fits obtained from a grid of **PHOENIX** models spanning a 2000 K range yield angular diameter differences of only 0.007 mas, 0.006 mas 0.004 mas at 500 nm, 800 nm, and 2.2 μm respectively; values comparable to the formal fit uncertainties. The atmosphere models in Table 5 yield different angular diameters because they have different temperature gradients, as shown in Figure 7.

The mean temperature structure of the 3-D **C0⁵BOLD** model and the 1-D **ATLAS 12** model “F” have shallower temperature gradients in the range $1 \leq \tau_{\text{ross}} \leq 5$ relative to the 1-D models without overshooting. This is expected because the radiative flux should be reduced when the convective flux is increased. Figure 8 shows the fraction of radiative flux as a function of optical depth for these models. The mean 3-D model and the 1-D model with overshooting have only $\sim 80\%$ of their total flux in radiation at $\tau_{\text{ross}} = 1$. At depths $\tau_{\text{ross}} \lesssim 8$ the mean 3-D and the 1-D overshooting radiative flux structures are quite similar. These best fitting models to the interferometric data show significant convective flux at $\tau_{\text{ross}} \lesssim 1$ and we conclude that the interferometric data provide evidence for convective overshooting in Procyon’s atmosphere.

The shallower temperature gradient introduced by overshooting reduces the relative limb darkening between 500 nm and 2.2 μm . This accounts for the variation in the best fit θ_{LD} values for models with different convection treatments. An analysis of the contribution functions, $S(\tau_{\lambda})e^{-\tau_{\lambda}}$, at the three wavelengths shows the 500 nm continuum forms in a range of depths partially below the depths forming the 800 nm continuum. The 800 nm band lies near the peak of the bound-free H⁻ opacity, the dominant continuum opacity in the optical. At 2.2 μm the H⁻ opacity, here free-free beyond the 1.6 μm H⁻ opacity minimum, is less than at 800 nm and similar to the 500 nm opacity. However, at 2.2 μm the intensity is much less sensitive to the temperature of Planckian radiation than at 500 nm. For the Sun, it was pointed out by Gingerich et al. (1971) that the lack of a steeply rising Planck function (with temperature) at 1.6 μm means that the intensities emerging from the hot convective layers are better probed at wavelengths immediately to the red of the Balmer limit (365 nm) even if the optical depth is a factor of two larger there than at the 1.6 μm opacity minimum. In short, similar depths are probed by the 500 nm and 2.2 μm bands, but the radiation field is much more sensitive the temperature gradient at 500 nm compared to 2.2 μm .

One-dimensional models without overshooting cannot be made more consistent with the multiwavelength visibility data by adjusting the mixing length parameter α . Based on the two stand-alone **PHOENIX** models “A” and “B” (see Table 5), changing α from 1.25 to 0.5 has no

effect on the derived angular diameters at 800 nm and 2.2 μm . At 500 nm the two best fit angular diameters differ by 0.35%. Note that model “B” with $\alpha = 0.5$ yields a slightly larger angular diameter at 500 nm relative to the $\alpha = 1.25$ model. Thus, reducing α slightly increases the degree of limb darkening for a model which is already too limb darkened compared to the observations presented here.

5.3. Photometry and 1-D Overshooting

As discussed above, we find that the 1-D ATLAS 12 model “F” with 50% overshooting fits the visibility data as well as the 3-D CO⁵BOLD model and that the two models have similar mean temperature gradients. However, models with mixing-length theory convection and overshooting have been subject to extensive comparisons with photometry, with the results favoring models without overshooting (Castelli et al. 1997; Smalley & Kupka 1997). In general, 1-D convection treatments (e.g. mixing-length variants, turbulent convection) for model stellar atmospheres with otherwise identical parameters yield different SEDs. Strömgren photometric indices are often employed to facilitate the comparison of these different synthetic SEDs with a large number of real SEDs. Such studies (Heiter et al. 2002, and references therein) generally find that 1-D atmosphere models with no overshooting and $\alpha = 0.5$ more closely reproduce the colors of real atmospheres relative to other 1-D models. This is demonstrated for Procyon by Smalley & Kupka (1997) who show that to reproduce the observed $(b - y)$ index with an ATLAS 9 overshooting model requires a model with $T_{\text{eff}} = 6830 \pm 142$ K (the uncertainty based on photometry alone), a value in excess of their derived interferometric value, $T_{\text{eff}} = 6560 \pm 130$ K. This confirms the findings of Castelli et al. (1997). These results appear to be strengthened by our more precise value for the interferometric T_{eff} value, now 6543 ± 87 K, based on the mean K-band angular diameter value (see Table 7). Now the best fit 1-D overshooting model to the photometry would appear to require a model T_{eff} value even more inconsistent with the interferometric T_{eff} .

Heiter et al. (2002) find that reducing the mixing-length parameter α in ATLAS 9 models yields synthetic indices more consistent with observations. Our comparisons suggest that 1-D models with lower α values better match photometry because this better approximates the composite SED in the b - and v -bands. As a result, constraining the 1-D α parameter with Strömgren photometry most likely constrains not the temperature structure of the 1-D model, but instead reflects the lack of hotter temperature components in the 1-D model, the same components responsible for the continuum below 160 nm.

The composite SED models reproduce photometric indices quite close to the observed values and match fairly well the full UV continuum flux distribution. On the basis of the spatially and temporally averaged 3-D radiative flux structure (Figure 8) one might guess a much redder $(b - y)$ color for this model because of the similarly to ATLAS 12 model “F”. However, unlike the 1-D case, in the 3-D case the distribution of surface temperatures suppresses the one-to-one connection between the mean photospheric SED and the mean temperature structure. Both composite models predict $(b - y)$ values slightly redder than observed, but much more consistent than the

1-D overshooting models. A slightly warmer CO⁵BOLD model ($T_{\text{eff}} = 6550$ K instead of 6500 K), more consistent with the interferometric value 6543 K, is expected to yield a slightly warmer distribution of temperatures and hence a bluer $(b - y)$. A more consistent modeling approach, where the colors are computed directly from the 3-D model intensities, should clearly be pursued once the wavelength-dependent opacities in 3-D models improve.

6. SUMMARY

We find that the multiwavelength visibility measurements of Procyon obtained by the Mark III and the VLTI interferometers characterize the mean temperature structure of its atmosphere while UV and optical spectrophotometry characterize the spatial distribution of surface temperatures expected from granulation on its surface. We find that predictions from a three-dimensional CO⁵BOLD hydrodynamic model atmosphere of Procyon match the interferometric, spectrophotometric, and photometric observations simultaneously, providing confidence in 3-D model predictions which until now had been tested predominantly with high-resolution spectroscopy. Based on 3-D and 1-D model comparisons, the interferometric data are consistent with a temperature structure with significant convective overshooting. While a 1-D model atmosphere with some overshooting matches the interferometric data, all 1-D models fail to match Procyon’s spectral energy distribution, most evidently below 160 nm. Strömgren photometric indices appear to be sensitive to the multicomponent brightness temperature distribution on Procyon’s surface. This would seem to severely complicate conclusions regarding convection in similar stars based on 1-D model atmosphere comparisons to optical spectrophotometric data.

D. Mozurkewich kindly provided the Mark III visibility data. We thank R. L. Kurucz for computing the ATLAS 12 spectra and radiation fields and for critical comments. These data and models were vital for this project. Thanks to S. T. Ridgway and S. N. Shore for their careful readings of the manuscript and for helpful discussions. I. Hubeny kindly provided critical comments. Thanks to A. Mérand for many helpful discussions and correspondence. Thanks to our anonymous referee for comments regarding the interferometric calibrations and for improving the organization of the paper. Thanks to the PHOENIX development team for their support and interest in this work. This work was performed in part under contract with the Jet Propulsion Laboratory (JPL) funded by NASA through the Michelson Fellowship Program. JPL is managed for NASA by the California Institute of Technology. NOAO is operated by AURA, Inc, under cooperative agreement with the National Science Foundation. HGL acknowledges financial support by the Swedish Research Council and the Royal Physiographic Society in Lund. The VLTI is operated by the European Southern Observatory at Cerro Paranal, Chile. The Mark III was funded by the Office of Naval Research and the Oceanographer of the Navy. This research has made use of NASA’s Astrophysics Data System, SIMBAD database, operated at CDS, Strasbourg, France. Some of the data presented in this paper was obtained from the Multimission Archive at the Space Telescope Science Institute (MAST). STScI

is operated by the Association of Universities for Research in Astronomy, Inc., under NASA contract NAS5-26555. Support for MAST for non-HST data is provided

by the NASA Office of Space Science via grant NAG5-7584 and by other grants and contracts.

REFERENCES

Abe, F., Bennett, D. P., Bond, I. A., Calitz, J. J., Claret, A., Cook, K. H., Furuta, Y., Gal-Yam, A., Glicenstein, J.-F., Hearnshaw, J. B., Hauschildt, P. H., Kent, D., Kilmartin, P. M., Kurata, Y., Masuda, K., Maoz, D., Matsubara, Y., Meintjes, P. J., Moniez, M., Muraki, Y., Noda, S., Ofek, E. O., OkaJima, K., Philpott, L., Rattenbury, N. J., Rhie, S. H., Sako, T., Sullivan, D. J., Sumi, T., Terndrup, D. M., Tristram, P. J., Yanagisawa, T., & Yock, P. C. M. 2003, *A&A*, 411, L493

Allende Prieto, C., Asplund, M., López, R. J. G., & Lambert, D. L. 2002, *ApJ*, 567, 544

Anders, E. & Grevesse, N. 1989, *Geochim. Cosmochim. Acta*, 53, 197

Asplund, M., Grevesse, N., Sauval, A. J., Allende Prieto, C., & Kiselman, D. 2004, *A&A*, 417, 751

Asplund, M., Gustafsson, B., Kiselman, D., & Eriksson, K. 1997, *A&A*, 318, 521

Asplund, M., Nordlund, Å., & Trampedach, R. 1999, in *ASP Conf. Ser. 173: Theory and Tests of Convection in Stellar Structure*, 221

Baschek, B., Scholz, M., & Wehrse, R. 1991, *A&A*, 246, 374

Bessell, M. S. & Brett, J. M. 1988, *PASP*, 100, 1134

Bohlin, R. C. 1996, *AJ*, 111, 1743

Bohlin, R. C. & Gilliland, R. L. 2004, *AJ*, 127, 3508

Castelli, F., Gratton, R. G., & Kurucz, R. L. 1997, *A&A*, 318, 841

Chaboyer, B., Demarque, P., & Guenther, D. B. 1999, *ApJ*, 525, L41

Claret, A. 2000, *A&A*, 363, 1081

Code, A. D., Davis, J., Bless, R. C., & Hanbury Brown, R. 1976, *ApJ*, 203, 417

Cohen, M., Walker, R. G., Carter, B., Hammersley, P., Kidger, M., & Noguchi, K. 1999, *AJ*, 117, 1864

Crawford, D. L. & Barnes, J. V. 1970, *AJ*, 75, 978

Cunha, K., Smith, V. V., Boesgaard, A. M., & Lambert, D. L. 2000, *ApJ*, 530, 939

Davis, J., Tango, W. J., & Booth, A. J. 2000, *MNRAS*, 318, 387

Fields, D. L., Albrow, M. D., An, J., Beaulieu, J.-P., Caldwell, J. A. R., DePoy, D. L., Dominik, M., Gaudi, B. S., Gould, A., Greenhill, J., Hill, K., Jørgensen, U. G., Kane, S., Martin, R., Menzies, J., Pogge, R. W., Pollard, K. R., Sackett, P. D., Sahu, K. C., Vermaak, P., Watson, R., Williams, A., Glicenstein, J.-F., & Hauschildt, P. H. 2003, *ApJ*, 596, 1305

Freytag, B., Steffen, M., & Dorch, B. 2002, *Astronomische Nachrichten*, 323, 213

Gingerich, O., Noyes, R. W., Kalkofen, W., & Cuny, Y. 1971, *Sol. Phys.*, 18, 347

Girard, T. M., Wu, H., Lee, J. T., Dyson, S. E., van Altena, W. F., Horch, E. P., Gilliland, R. L., Schaefer, K. G., Bond, H. E., Ftaclas, C., Brown, R. H., Toomey, D. W., Shipman, H. L., Provencal, J. L., & Pourbaix, D. 2000, *AJ*, 119, 2428

Glindemann, A., Alameda, J., Amestica, R., Ballester, P., Bauvir, B., Bugueno, E., Correia, S., Delgado, F., Delplancke, F., Derie, F., Duhoux, P., di Folco, E., Gennai, A., Gilli, B., Giordano, P., Gitton, P. B., Guisard, S., Housen, N., Huxley, A., Kervella, P., Kiekebusch, M., Koehler, B., Leveque, S. A., Longinotti, A., Morel, S., Paresce, F., Duc, T. P., Richichi, A., Schoeller, M., Tarenghi, M., Wallander, A., Wittkowski, M., & Wilhelm, R. 2003, in *Interferometry for Optical Astronomy II*. Edited by Wesley A. Traub. *Proceedings of the SPIE*, Volume 4838, 89–100

Glushneva, I. N., Kharitonov, A. V., Kniazeva, L. N., & Shenavrin, V. I. 1992, *A&AS*, 92, 1

Gray, R. O., Napier, M. G., & Winkler, L. I. 2001, *AJ*, 121, 2148

Gustafsson, B., Bell, R. A., Eriksson, K., & Nordlund, A. 1975, *A&A*, 42, 407

Hanbury Brown, R., Davis, J., & Allen, L. R. 1974, *MNRAS*, 167, 121

Hauschildt, P. H., Allard, F., Ferguson, J., Baron, E., & Alexander, D. R. 1999, *ApJ*, 525, 871

Hauschildt, P. H. & Baron, E. 1999, *J. Comp. and App. Math.*, 109, 41

Heiter, U., Kupka, F., van't Veer-Menneret, C., Barban, C., Weiss, W. W., Goupil, M.-J., Schmidt, W., Katz, D., & Garrido, R. 2002, *A&A*, 392, 619

Johnson, H. L. 1965, *Communications of the Lunar and Planetary Laboratory*, 3, 73

Keenan, P. C. 1938, *ApJ*, 87, 45

Kervella, P., Gitton, P. B., Segransan, D., di Folco, E., Kern, P. Y., Kiekebusch, M., Duc, T. P., Longinotti, A., Coude du Foresto, V., Ballester, P., Sabet, C., Cotton, W. D., Schoeller, M., & Wilhelm, R. 2003a, in *Interferometry for Optical Astronomy II*. Edited by Wesley A. Traub. *Proceedings of the SPIE*, Volume 4838, 858–869

Kervella, P., Segransan, D., & Coudé du Foresto, V. 2004a, *A&A*, 425, 1161

Kervella, P., Thévenin, F., Morel, P., Berthomieu, G., Bordé, P., & Provost, J. 2004b, *A&A*, 413, 251

Kervella, P., Thévenin, F., Morel, P., Bordé, P., & Di Folco, E. 2003b, *A&A*, 408, 681

Kiehling, R. 1987, *A&AS*, 69, 465

Koutchmy, S., Koutchmy, O., & Kotov, V. 1977, *A&A*, 59, 189

Kurucz, R. L. 1979, *ApJS*, 40, 1

Kurucz, R. L. 1992, *Rev. Mex. Astron. Astrofis.*, 23, 187

Lester, J. B., Gray, R. O., & Kurucz, R. L. 1986, *ApJS*, 61, 509

Ludwig, H.-G. 1992, PhD thesis, University of Kiel

Ludwig, H.-G., Allard, F., & Hauschildt, P. H. 2002, *A&A*, 395, 99

Münch, G. 1945, *ApJ*, 102, 385

Martié, M., Schmitt, J., Lebrun, J.-C., Barban, C., Connes, P., Bouchy, F., Michel, E., Baglin, A., Appourchaux, T., & Bertaux, J.-L. 1999, *A&A*, 351, 993

Matsushima, S. 1969, *ApJ*, 158, 1137

Matthews, J. M., Kusching, R., Guenther, D. B., Walker, G. A. H., Moffat, A. F. J., Rucinski, S. M., Sasselov, D., & Weiss, W. W. 2004, *Nature*, 430, 51

Mihalas, D. 1978, *Stellar Atmospheres*, 2nd edn. (San Francisco: Freeman)

Milne, E. A. 1921, *MNRAS*, 81, 361

Morel, M. & Magnenat, P. 1978, *A&AS*, 34, 477+

Mozurkewich, D., Armstrong, J. T., Hindsley, R. B., Quirrenbach, A., Hummel, C. A., Hutter, D. J., Johnston, K. J., Hajian, A. R., Elias, N. M., Buscher, D. F., & Simon, R. S. 2003, *AJ*, 126, 2502

Mozurkewich, D., Johnston, K. J., Simon, R. S., Bowers, P. F., Gaume, R., Hutter, D. J., Colavita, M. M., Shao, M., & Pan, X. P. 1991, *AJ*, 101, 2207

Neckel, H. & Labs, D. 1994, *Sol. Phys.*, 153, 91

Nordström, B., Mayor, M., Andersen, J., Holmberg, J., Pont, F., Jørgensen, B. R., Olsen, E. H., Udry, S., & Mowlavi, N. 2004, *A&A*, 418, 989

Ohishi, N., Nordgren, T. E., & Hutter, D. J. 2004, *ApJ*, 612, 463

Payne, C. H. 1925, *Stellar Atmospheres*, ed. H. Shapley, *Harvard Observatory Monographs No. 1* (Cambridge: Harvard Observatory)

Perrin, G., Ridgway, S. T., Coudé du Foresto, V., Mennesson, B., Traub, W. A., & Lacasse, M. G. 2004, *A&A*, 418, 675

Perryman, M. A. C., Lindegren, L., Kovalevsky, J., Hoeg, E., Bastian, U., Bernacca, P. L., Crézé, M., Donati, F., Grenon, M., van Leeuwen, F., van Der Marel, H., Mignard, F., Murray, C. A., Le Poole, R. S., Schrijver, H., Turon, C., Arenou, F., Froeschlé, M., & Petersen, C. S. 1997, *A&A*, 323, L49

Plaskett, H. H. 1936, *MNRAS*, 96, 402

Robinson, F. J., Demarque, P., Li, L. H., Sofia, S., Kim, Y.-C., Chan, K. L., & Guenther, D. B. 2003, *MNRAS*, 340, 923

—. 2004, *MNRAS*, 347, 1208

Rodríguez-Pascual, P. M., González-Riestra, R., Schartel, N., & Wamsteker, W. 1999, *A&AS*, 139, 183

Schwarzschild, K. 1966, in *Selected Papers on the Transfer of Radiation*, ed. D. H. Menzel (New York: Dover), *Über das Gleichgewicht der Sonnenatmosphäre*“ Nachrichten von der Königlichen Gesellschaft der Wissenschaften zu Göttingen. Math.-phys. Klassse (1906) 295, 41

Shao, M., Colavita, M. M., Hines, B. E., Staelin, D. H., & Hutter, D. J. 1988, *A&A*, 193, 357

Short, C. I. & Hauschildt, P. H. 2005, *ApJ*, 618, 926

Smalley, B. & Kupka, F. 1997, A&A, 328, 349

Spiegel, E. A. 1963, ApJ, 138, 216

Stein, R. F. & Nordlund, A. 1998, ApJ, 499, 914

Strömgren, B. 1966, ARA&A, 4, 433

Swihart, T. L. 1956, ApJ, 123, 143

Travis, L. D. & Matsushima, S. 1968, ApJ, 154, 689

—. 1973, ApJ, 180, 975

Unsöld, A. 1930, Zeitschrift für Astrophysics, 1, 138

Vernazza, J. E., Avrett, E. H., & Loeser, R. 1976, ApJS, 30, 1

Wedemeyer, S., Freytag, B., Steffen, M., Ludwig, H.-G., & Holweger, H. 2004, A&A, 414, 1121

Wildt, R. 1939, ApJ, 90, 611

Wittkowski, M., Aufdenberg, J. P., & Kervella, P. 2004, A&A, 413, 711

Wood, B. E., Harper, G. M., Linsky, J. L., & Dempsey, R. C. 1996, ApJ, 458, 761

Woolley, R. V. D. R. 1941, MNRAS, 101, 52

TABLE 1
 VLTI/VINCI K-BAND VISIBILITY MEASUREMENTS

Julian Date	Projected Baseline (meters)	Position Angle (degrees)	$V^2 \times 100$	$\sigma V_{\text{stat}}^2 \times 100$	$\sigma V_{\text{sys}}^2 \times 100$	$\sigma V_{\text{total}}^2 \times 100$	Calibration Star
2452674.59969	21.900	73.45	83.01	1.90	0.12	1.90	α CMa
2452674.60482	22.192	73.51	83.50	2.20	0.12	2.21	α CMa
2452674.60889	22.409	73.54	83.76	2.18	0.12	2.18	α CMa
2452672.72358	23.005	70.29	81.90	1.31	0.08	1.31	α CMa
2452682.69435	23.081	70.42	86.17	3.20	0.07	3.20	α CMa
2452685.68579	23.095	70.45	84.07	1.86	0.08	1.86	α CMa
2452671.72379	23.104	70.46	84.09	3.61	0.07	3.61	α CMa
2452681.69611	23.118	70.49	84.93	3.86	0.08	3.87	α CMa
2452672.72041	23.129	70.50	83.48	1.13	0.08	1.14	α CMa
2452683.68954	23.160	70.56	84.70	2.88	0.09	2.88	α CMa
2452682.69041	23.227	70.68	83.64	3.12	0.07	3.12	α CMa
2452681.69192	23.271	70.76	83.88	3.81	0.08	3.81	α CMa
2452679.69711	23.280	70.77	81.32	3.88	0.23	3.89	α CMa
2452671.71859	23.293	70.80	82.83	3.40	0.07	3.40	α CMa
2452683.68469	23.331	70.87	82.44	2.73	0.09	2.73	α CMa
2452682.68572	23.386	70.97	80.90	3.01	0.07	3.01	α CMa
2452679.69316	23.410	71.01	83.33	2.38	0.23	2.39	α CMa
2452671.71484	23.415	71.02	82.49	2.19	0.07	2.20	α CMa
2452683.68116	23.443	71.08	82.54	2.71	0.09	2.71	α CMa
2452671.70658	23.644	71.48	80.91	2.43	0.07	2.43	α CMa
2452671.70225	23.741	71.71	81.93	2.43	0.07	2.43	α CMa
2452684.66566	23.764	71.76	83.54	2.51	0.09	2.51	α CMa
2452685.66048	23.810	71.88	83.32	1.83	0.09	1.84	α CMa
2452684.62226	23.819	73.24	80.76	2.43	0.08	2.43	α CMa
2452671.69791	23.824	71.91	85.10	2.57	0.07	2.57	α CMa
2452684.66129	23.842	71.96	82.11	2.47	0.08	2.47	α CMa
2452685.65611	23.879	72.07	82.65	1.71	0.09	1.72	α CMa
2452683.62916	23.884	73.15	82.34	2.74	0.09	2.74	α CMa
2452684.62693	23.891	73.14	84.20	2.66	0.09	2.66	α CMa
2452682.66269	23.901	72.15	80.19	2.99	0.07	2.99	α CMa
2452684.65703	23.903	72.15	82.22	2.47	0.08	2.47	α CMa
2452671.69151	23.915	72.20	82.27	2.16	0.07	2.16	α CMa
2452685.65156	23.934	72.27	80.65	1.68	0.09	1.68	α CMa
2452683.63367	23.938	73.04	82.01	2.76	0.09	2.76	α CMa
2452684.63099	23.938	73.04	80.15	2.72	0.08	2.72	α CMa
2452682.65863	23.945	72.31	82.83	3.08	0.07	3.08	α CMa
2452672.68439	23.958	72.37	81.00	1.13	0.08	1.13	α CMa
2452674.67842	23.962	72.39	81.05	1.80	0.10	1.81	α CMa
2452683.65385	23.962	72.39	83.33	2.78	0.09	2.78	α CMa
2452683.63773	23.971	72.93	81.89	2.80	0.09	2.80	α CMa
2452682.65360	23.981	72.50	80.45	3.00	0.07	3.00	α CMa
2452684.64797	23.981	72.51	82.02	2.47	0.08	2.48	α CMa
2452685.63493	23.985	72.85	82.08	1.94	0.09	1.94	α CMa
2452683.64960	23.986	72.55	83.19	2.78	0.09	2.78	α CMa
2452674.67396	23.987	72.56	81.92	1.82	0.10	1.82	α CMa
2452672.67922	23.988	72.56	79.78	1.16	0.08	1.16	α CMa
2452685.64373	23.988	72.56	79.08	1.91	0.08	1.91	α CMa
2452684.63971	23.991	72.79	81.00	2.43	0.08	2.44	α CMa
2452684.64410	23.993	72.65	81.56	2.45	0.08	2.45	α CMa
2452672.67394	23.994	72.74	80.85	1.10	0.08	1.10	α CMa
2452674.67012	23.995	72.69	81.18	1.80	0.10	1.80	α CMa
2452683.64541	23.995	72.69	81.71	2.72	0.09	2.72	α CMa
2452685.63998	23.995	72.69	79.22	1.68	0.08	1.68	α CMa
2453002.63052	42.518	69.88	54.52	1.23	0.22	1.25	30 Gem
2453002.63564	43.943	70.39	51.89	1.16	0.21	1.18	30 Gem
2453002.66192	50.648	72.27	40.22	0.51	0.18	0.54	30 Gem
2453002.66734	51.889	72.53	36.85	0.71	0.16	0.73	30 Gem
2452339.59761	55.734	147.99	32.92	1.33	0.44	1.40	α CMa
2452339.59331	56.237	147.32	29.39	0.99	0.40	1.07	α CMa
2452339.58907	56.731	146.69	31.28	1.11	0.42	1.18	α CMa
2453002.69427	57.239	73.37	28.79	0.50	0.13	0.52	30 Gem
2453029.62077	57.277	73.37	29.14	2.01	0.10	2.02	18 Mon
2453002.69950	58.111	73.45	27.98	0.48	0.13	0.50	30 Gem
2453029.62595	58.137	73.45	27.79	1.92	0.10	1.92	18 Mon
2452994.73707	60.383	73.58	25.89	0.45	0.15	0.47	HR 1799
2453002.72628	61.657	73.57	22.37	0.73	0.09	0.73	18 Mon
2453002.73158	62.172	73.54	22.10	1.05	0.09	1.06	18 Mon
2452996.75146	62.477	73.51	22.06	0.25	0.08	0.27	6 Leo
2452996.75644	62.863	73.45	21.48	0.26	0.08	0.27	6 Leo
2452995.76035	62.946	73.43	21.06	0.33	0.08	0.34	6 Leo
2452996.81799	62.952	71.42	21.44	0.33	0.11	0.34	6 Leo
2452995.81464	63.326	71.74	20.80	0.27	0.10	0.28	6 Leo
2452996.81167	63.339	71.75	20.41	0.27	0.10	0.29	6 Leo

TABLE 1 — *Continued*

Julian Date	Projected Baseline (meters)	Position Angle (degrees)	$V^2 \times 100$	$\sigma V_{\text{stat}}^2 \times 100$	$\sigma V_{\text{sys}}^2 \times 100$	$\sigma V_{\text{total}}^2 \times 100$	Calibration Star
2452995.80179	63.845	72.31	20.26	0.27	0.10	0.29	6 Leo
2452996.78120	63.942	72.93	19.80	0.18	0.08	0.20	6 Leo
2453002.76593	63.957	72.89	20.05	0.59	0.08	0.60	18 Mon
2452996.78597	63.988	72.78	19.85	0.20	0.08	0.22	6 Leo
2453002.77184	63.991	72.71	19.88	0.66	0.08	0.66	18 Mon

TABLE 2
MARK III 500 NM VISIBILITY MEASUREMENTS

Julian Date	Projected Baseline (meters)	Position Angle (degrees)	V^2	$\sigma V_{\text{total}}^2$
2447452.956	2.803	23.049	1.024	0.106
2447452.970	2.768	20.864	0.900	0.089
2447452.986	2.728	17.918	0.944	0.072
2447453.004	2.689	14.543	0.966	0.073
2447453.041	2.630	6.448	1.013	0.075
2447453.924	2.877	27.258	0.859	0.058
2447453.936	2.847	25.646	0.911	0.049
2447453.949	2.814	23.750	0.984	0.051
2447453.962	2.781	21.688	0.904	0.046
2447453.981	2.734	18.425	0.940	0.048
2447454.921	5.093	27.288	0.894	0.053
2447454.957	4.934	22.135	0.780	0.046
2447454.969	4.878	20.047	0.804	0.048
2447454.980	4.833	18.154	0.884	0.051
2447454.993	4.778	15.552	0.933	0.054
2447455.003	4.741	13.490	0.925	0.054
2447455.015	4.705	11.116	0.927	0.054
2447455.024	4.680	9.063	0.954	0.055
2447455.037	4.653	6.184	0.831	0.051
2447455.050	4.636	3.183	0.893	0.052
2447455.910	6.686	28.266	0.578	0.048
2447455.928	6.587	25.979	0.730	0.057
2447455.945	6.490	23.593	0.659	0.052
2447455.962	6.384	20.683	0.762	0.059
2447455.974	6.319	18.661	0.694	0.053
2447455.985	6.258	16.546	0.755	0.057
2447455.996	6.204	14.363	0.802	0.061
2447456.007	6.155	12.079	0.828	0.063
2447456.018	6.114	9.724	0.836	0.064
2447456.030	6.079	7.157	0.826	0.063
2447456.041	6.055	4.478	0.800	0.061
2447456.916	22.193	27.143	0.010	0.002
2447456.935	21.836	24.598	0.016	0.003
2447457.046	20.215	2.793	0.035	0.009
2447457.964	21.220	19.514	0.020	0.002
2447457.976	20.984	17.152	0.024	0.003
2447457.993	20.703	13.805	0.031	0.002
2447458.008	20.505	10.815	0.030	0.002
2447458.019	20.377	8.311	0.032	0.002
2447458.034	20.256	4.843	0.033	0.002
2447458.044	20.213	2.678	0.038	0.002
2447458.053	20.195	0.435	0.040	0.002
2447460.952	29.068	20.149	0.006	0.002
2447460.970	28.613	16.858	0.003	0.002

TABLE 3
 MARK III 800 NM VISIBILITY MEASUREMENTS

Julian Date	Projected Baseline (meters)	Position Angle (degrees)	V^2	$\sigma V_{\text{total}}^2$
2447452.956	2.803	23.048	1.016	0.049
2447452.970	2.768	20.863	0.948	0.043
2447452.986	2.728	17.918	1.009	0.037
2447453.004	2.689	14.544	0.988	0.035
2447453.022	2.656	10.718	0.997	0.035
2447453.041	2.630	6.447	1.015	0.036
2447453.924	2.877	27.260	0.964	0.042
2447453.936	2.847	25.647	0.968	0.029
2447453.949	2.814	23.750	1.003	0.030
2447453.962	2.781	21.688	0.963	0.028
2447453.981	2.734	18.423	0.970	0.027
2447454.921	5.093	27.288	0.964	0.027
2447454.957	4.934	22.135	0.908	0.026
2447454.969	4.878	20.049	0.919	0.026
2447454.980	4.833	18.155	0.967	0.026
2447454.993	4.778	15.552	0.986	0.027
2447455.003	4.741	13.491	0.978	0.027
2447455.015	4.705	11.115	0.972	0.027
2447455.024	4.680	9.062	0.977	0.026
2447455.037	4.653	6.185	0.933	0.032
2447455.050	4.636	3.183	0.960	0.027
2447455.928	6.587	25.980	0.881	0.030
2447455.945	6.490	23.593	0.845	0.030
2447455.962	6.384	20.683	0.899	0.030
2447455.974	6.319	18.661	0.856	0.029
2447455.985	6.258	16.546	0.900	0.030
2447455.996	6.204	14.363	0.920	0.030
2447456.007	6.155	12.078	0.922	0.031
2447456.018	6.114	9.724	0.941	0.031
2447456.030	6.079	7.157	0.939	0.031
2447456.041	6.055	4.478	0.928	0.030
2447438.947	18.608	29.260	0.364	0.013
2447438.968	18.309	26.817	0.380	0.012
2447438.988	17.984	23.980	0.395	0.012
2447439.024	17.413	17.976	0.415	0.013
2447439.043	17.146	14.289	0.438	0.014
2447456.916	22.193	27.143	0.244	0.006
2447456.935	21.836	24.598	0.250	0.006
2447457.046	20.215	2.793	0.320	0.016
2447457.964	21.220	19.514	0.271	0.006
2447457.976	20.984	17.152	0.290	0.007
2447457.993	20.703	13.805	0.306	0.006
2447458.008	20.505	10.815	0.312	0.006
2447458.019	20.377	8.311	0.307	0.007
2447458.034	20.256	4.843	0.335	0.007
2447458.044	20.213	2.678	0.332	0.007
2447458.053	20.195	0.435	0.335	0.007
2447460.952	29.068	20.149	0.068	0.003
2447460.970	28.613	16.858	0.079	0.004
2447478.899	26.960	20.833	0.108	0.007
2447478.935	26.154	14.128	0.125	0.009
2447478.950	25.887	11.006	0.139	0.010
2447478.965	25.679	7.698	0.149	0.010
2447484.836	28.099	27.661	0.077	0.016
2447484.867	27.366	23.477	0.103	0.010
2447484.878	27.077	21.631	0.121	0.015
2447484.884	26.926	20.595	0.103	0.011
2447484.891	26.773	19.497	0.117	0.014
2447484.897	26.630	18.398	0.120	0.017
2447484.939	25.806	9.841	0.143	0.013
2447484.951	25.659	7.303	0.147	0.015
2447484.962	25.552	4.594	0.146	0.014
2447484.974	25.493	1.879	0.143	0.012
2447484.981	25.482	0.339	0.154	0.013
2447484.987	25.486	-1.146	0.135	0.011
2447484.993	25.502	-2.497	0.124	0.016
2447833.958	24.330	14.949	0.184	0.002
2447833.974	24.055	11.678	0.197	0.003
2447833.983	23.923	9.706	0.209	0.003
2447833.989	23.855	8.511	0.202	0.003
2447833.997	23.767	6.625	0.206	0.003
2447834.002	23.722	5.442	0.209	0.003
2447834.011	23.670	3.558	0.217	0.005

TABLE 3 — *Continued*

Julian Date	Projected Baseline (meters)	Position Angle (degrees)	V^2	$\sigma V_{\text{total}}^2$
2447834.024	23.632	0.512	0.214	0.004
2447834.029	23.633	-0.749	0.198	0.004
2447834.036	23.648	-2.353	0.208	0.003
2447834.042	23.673	-3.700	0.203	0.004
2447834.049	23.715	-5.208	0.205	0.003
2447834.055	23.766	-6.598	0.207	0.006
2447834.061	23.831	-8.048	0.182	0.007

TABLE 4
SYNTHETIC STRÖMGREN INDICES FOR COMPOSITE SED COMPONENTS

Surface Area Weight	$T_{\text{eff}}(\text{K})$	$\log(g)$	α	$(b - y)$	c_1
Composite SED A, $\beta = 0.6$ linear limb darkening					
0.002	5483	3.95	1.25	0.452	0.469
0.027	5693	3.95	1.25	0.416	0.446
0.093	5893	3.95	1.25	0.384	0.436
0.125	6074	3.95	1.25	0.356	0.445
0.120	6241	3.95	1.25	0.332	0.464
0.108	6395	3.95	1.25	0.311	0.491
0.114	6538	3.95	1.25	0.291	0.521
0.134	6672	3.95	1.25	0.274	0.554
0.139	6799	3.95	1.25	0.257	0.586
0.106	6920	3.95	1.25	0.242	0.620
0.029	7034	3.95	1.25	0.227	0.652
0.002	7145	3.95	1.25	0.213	0.684
Composite SED B, $\beta = 0.5$ linear limb darkening					
0.002	5539	3.95	1.25	0.442	0.461
0.027	5751	3.95	1.25	0.406	0.444
0.093	5953	3.95	1.25	0.375	0.437
0.125	6136	3.95	1.25	0.347	0.451
0.120	6304	3.95	1.25	0.323	0.474
0.108	6460	3.95	1.25	0.302	0.504
0.114	6604	3.95	1.25	0.283	0.536
0.134	6740	3.95	1.25	0.265	0.571
0.139	6869	3.95	1.25	0.248	0.606
0.106	6990	3.95	1.25	0.233	0.639
0.029	7106	3.95	1.25	0.218	0.672
0.002	7217	3.95	1.25	0.205	0.704

TABLE 5
FIT ANGULAR DIAMETERS

Model	Parameters	Mark III 500 nm (mas)	Mark III 800 nm (mas)	VLTI/VINCI 2.2 μm (mas)
“A” PHOENIX	$T_{\text{eff}}=6530 \text{ K}$, $\log(g) = 3.95$, $\alpha = 1.25$	5.449 ± 0.012	5.416 ± 0.005	5.411 ± 0.006
“B” PHOENIX	$T_{\text{eff}}=6530 \text{ K}$, $\log(g) = 3.95$, $\alpha = 0.5$	5.468 ± 0.012	5.415 ± 0.005	5.410 ± 0.006
“C1” CO ⁵ BOLD + PHOENIX	$T_{\text{eff}}=6500 \text{ K}$, $\log(g) = 4.0$, global mean structure	5.387 ± 0.011	5.388 ± 0.005	5.402 ± 0.006
“C2” CO ⁵ BOLD + PHOENIX	$T_{\text{eff}}=6500 \text{ K}$, $\log(g) = 4.0$, 12 weighted structures	5.409 ± 0.011	5.393 ± 0.005	5.405 ± 0.006
“D” ATLAS 12	$T_{\text{eff}}=6530 \text{ K}$, $\log(g) = 3.95$, $\alpha = 1.25$, no overshooting	5.426 ± 0.011	5.404 ± 0.005	5.404 ± 0.006
“E” ATLAS 12	$T_{\text{eff}}=6530 \text{ K}$, $\log(g) = 3.95$, $\alpha = 1.25$, 100% overshooting	5.368 ± 0.011	5.383 ± 0.005	5.394 ± 0.006
“F” ATLAS 12	$T_{\text{eff}}=6530 \text{ K}$, $\log(g) = 3.95$, $\alpha = 1.25$, 50% overshooting	5.400 ± 0.011	5.398 ± 0.005	5.402 ± 0.006
“U” Uniform Disk	$V^2 = \left 2J_1(\pi\theta_{\text{UD}}B/\bar{\lambda})/(\pi\theta_{\text{UD}}B/\bar{\lambda}) \right ^2$	5.044 ± 0.010	5.208 ± 0.005	5.302 ± 0.005

TABLE 6
SYNTHETIC STRÖMGREN INDICES

Model	T_{eff} (K)	$\log(g)$	Additional Parameters	$(b - y)^a$	c_1^a
ATLAS 12 "E"	6530	3.95	$\alpha = 1.25$, overshooting	0.321	0.378
ATLAS 12 "F"	6530	3.95	$\alpha = 1.25$, 50% overshooting	0.311	0.402
ATLAS 12 "D"	6530	3.95	$\alpha = 1.25$, no overshooting	0.302	0.437
PHOENIX "A"	6530	3.95	$\alpha = 1.25$	0.292	0.519
PHOENIX "B"	6530	3.95	$\alpha = 0.50$	0.282	0.547
Composite SED A	6466	3.95	$\beta = 0.60$ linear limb darkening	0.293	0.539
Composite SED B	6531	3.95	$\beta = 0.50$ linear limb darkening	0.283	0.553

^a Interstellar reddening towards Procyon is assumed to be negligible: $(b - y) = (b - y)_0$, $c_1 = c_0$. Observed values: $(b - y) = 0.272$ (Crawford & Barnes 1970; Nordström et al. 2004) and $c_1 = 0.532$ (Crawford & Barnes 1970).

TABLE 7
FUNDAMENTAL PARAMETERS FOR PROCYON A

Parameter	Symbol	Value	Reference
Limb-darkened angular diameter (mas)	θ_{LD}	5.404 ± 0.031	Table 5, § 5
Bolometric flux (erg cm $^{-2}$ s $^{-1}$)	\mathcal{F}	$(17.86 \pm 0.89) \times 10^{-6}$	§ 2.2
Effective temperature (K)	T_{eff}	6543 ± 84	θ_{LD} and \mathcal{F}
Parallax (mas)	π	285.93 ± 0.88	Perryman et al. (1997)
Radius (R_{\odot})	R	2.031 ± 0.013	θ_{LD} and π
Mass (M_{\odot})	M	1.42 ± 0.04	Girard et al. (2000)
Surface gravity (cm s $^{-2}$)	$\log(g)$	3.975 ± 0.013	R and M

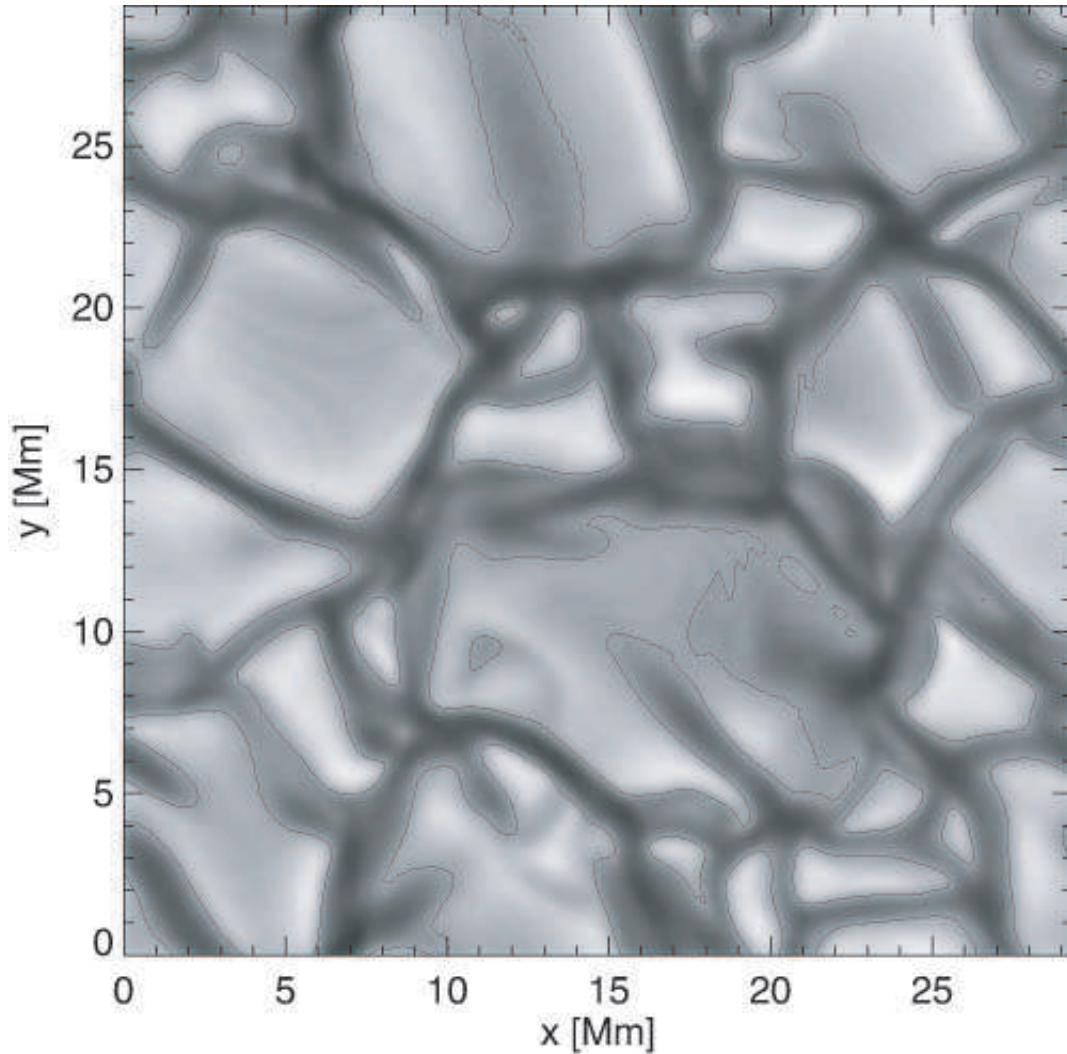


FIG. 1.— Typical map of the emergent white light intensity in vertical direction encountered during the temporal evolution of the grey C0⁵BOLD model. The black line depicts an isophote at $3.95 \times 10^{10} \text{ erg cm}^{-2} \text{ sr}^{-1} \text{ s}^{-1}$ approximately corresponding to the image's median intensity (see Figure 2).

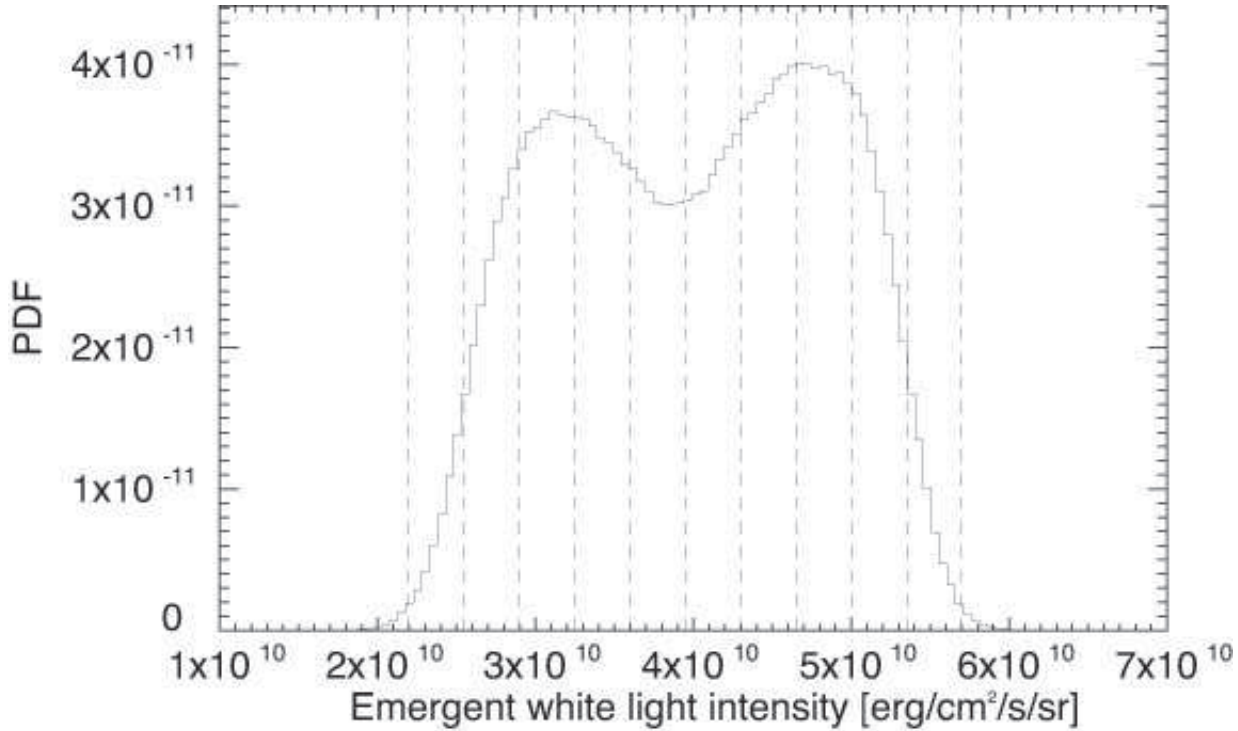


FIG. 2.— Probability density function (PDF), the probability per differential intensity interval with the units of inverse intensity, of the emergent white light intensity of the grey C05BOLD model. The PDF was derived from a sequence of intensity maps like the one shown in Figure 1. Twelve intensity intervals are demarcated by the dashed lines. The surface area weights for these intervals are given in Table 4.

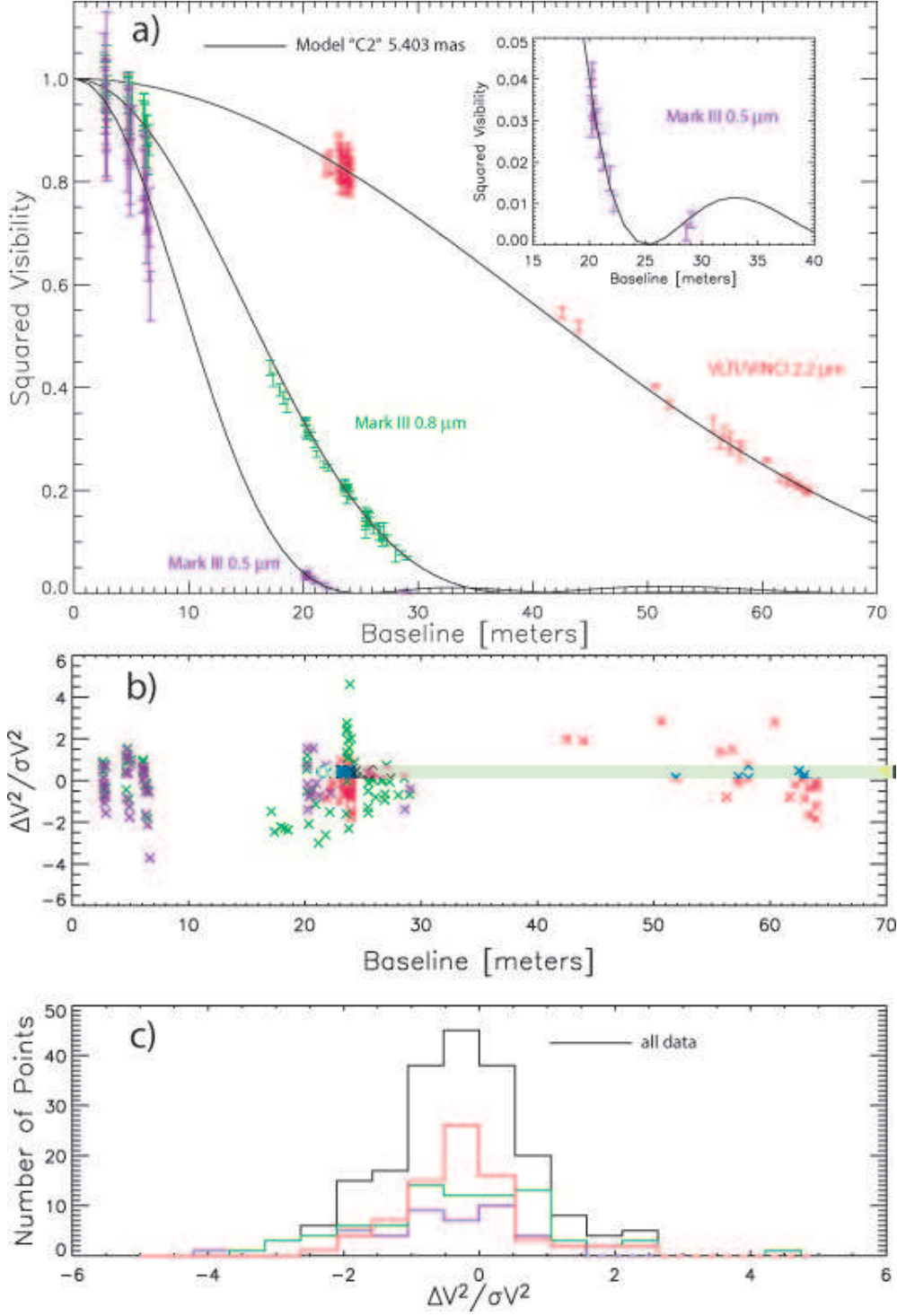


FIG. 3.— (a) The squared visibility data from Tables 1 (red), 2 (purple) and 3 (green) as a function of projected baseline compared to the synthetic visibilities (from eq.(2)) from the 3-D CO⁵BOLD + PHOENIX model “C2” with an angular diameter of 5.403 mas. (b) The deviations of each data set from the model. (c) Histograms of these deviations for each data set and for all the data combined.

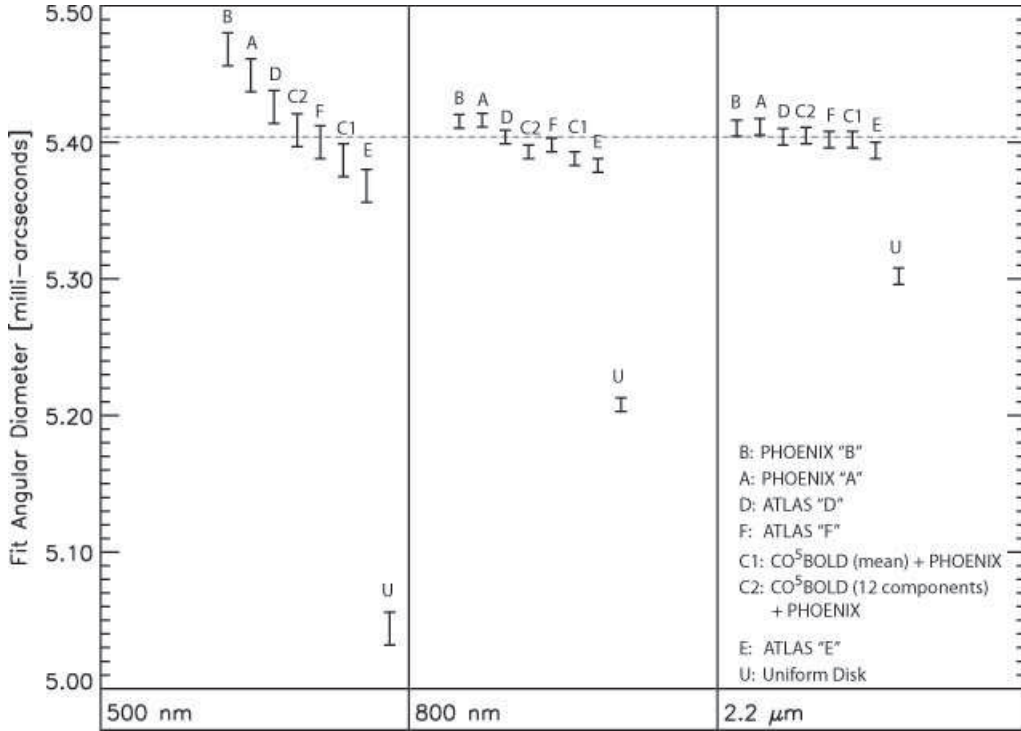


FIG. 4.— A comparison of the best fit angular diameters θ_{LD} at 500 nm, 800 nm (Mark III data), and 2.2 μ m (VLTI data) from Table 5 for the seven atmosphere models “A” to “F” and one uniform disk model “U”. The uniform disk angular diameters indicate that Procyon is more limb darkened at shorter wavelengths as expected. The atmosphere model fits are more dispersed at shorter wavelengths. The fits indicate that 1-D models without overshooting are too limb darkened at 500 nm, while 1-D model “E” with 100% overshooting is not limb darkened enough. Model “F” with 50% overshooting yield the same angular diameter (within 1σ) at all three wavelengths. The 3-D $CO^5BOLD + PHOENIX$ models “C1” and “C2” yield angular diameters slightly less consistent than model “F”, but with no free parameters for convection. The dashed line indicates the angular diameter of the model in Figure 3.

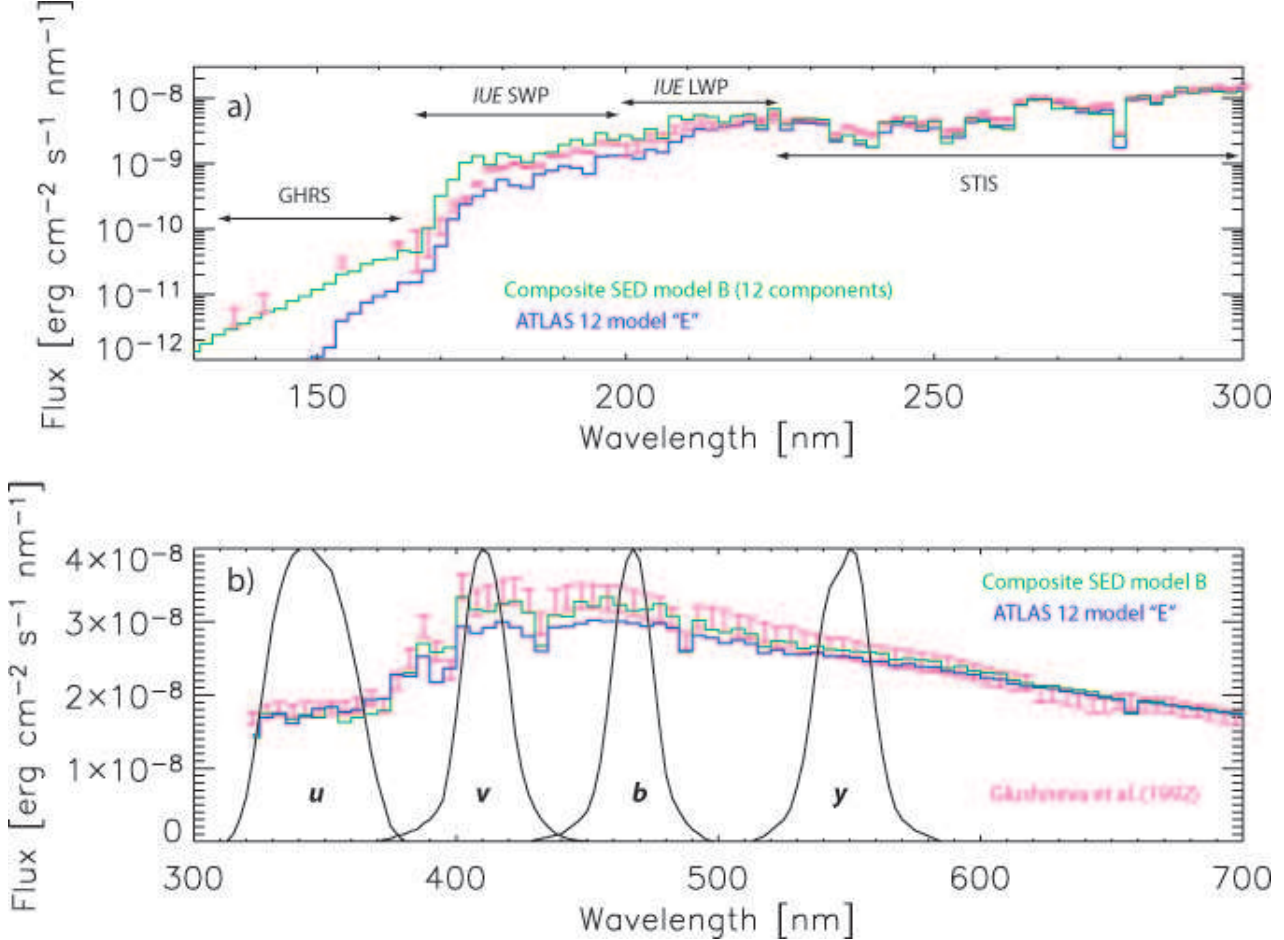


FIG. 5.— Comparisons between synthetic spectral energy distributions and spectrophotometric measurements at ultraviolet and visual wavelengths. The models and data are binned to 2 nm resolution in the UV for clarity. The models are binned to 5 nm in the visual to match the resolution of the spectrophotometry. The synthetic SEDs are scaled in absolute flux using an angular diameter of 5.40 mas, a value consistent with our best interferometric estimate (see Table 7). (a) Composite SED model B (green), which incorporates a 3-D model for the distribution of surface intensities due to granulation, better represents the UV flux distribution than a single T_{eff} component 1-D model (blue, ATLAS 12 model "E"), particularly at wavelengths below 160 nm, where all five single T_{eff} component, 1-D atmosphere models fail. (b) Composite SED model B (green) yields Strömgren v - and b -band fluxes consistent with the observed spectrophotometry (Glushneva et al. 1992) and larger than the 1- T_{eff} component model (blue, ATLAS 12 model "E"). These two models are in closer agreement in the u - and y -bands.

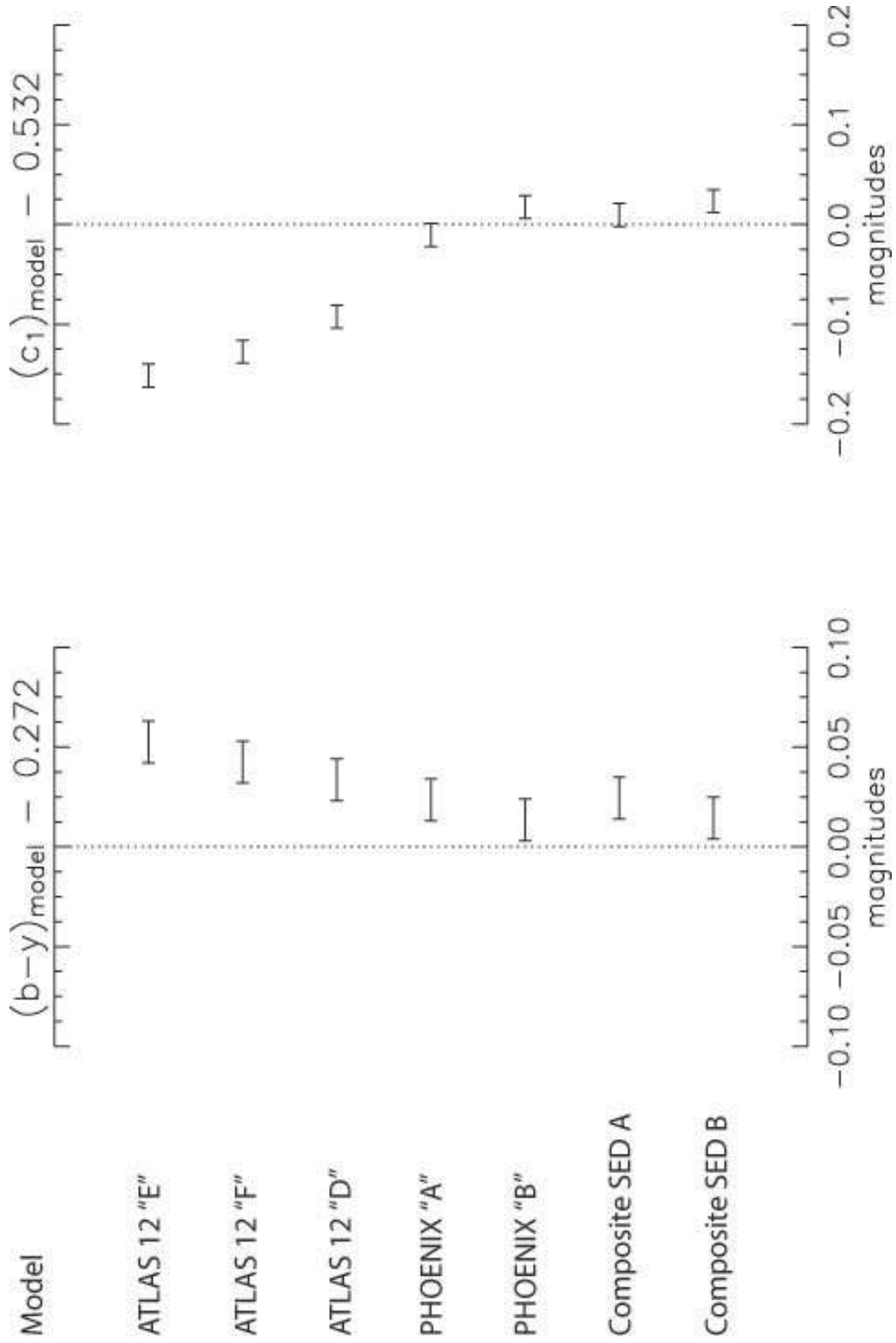


FIG. 6.—A comparison of the synthetic $(b-y)$ and c_1 Strömgren indices from Table 6 relative to the observed indices (Crawford & Barnes 1970).

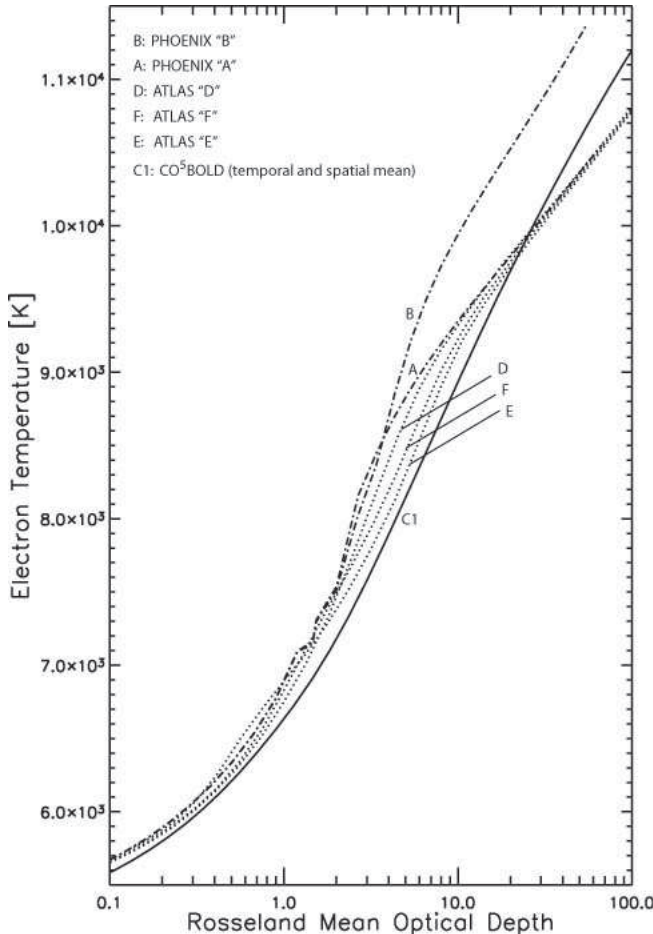


FIG. 7.— A comparison of six model atmosphere temperature on a mean Rosseland optical depth scale: PHOENIX models “A” and “B” (dash-dot), ATLAS 12 models “D”, “E”, “F” (dot), and CO^5BOLD model “C1” (solid). The degree of limb darkening, particularly at 500 nm where the opacity is relatively low compared to 800 nm and where the intensity contrast as a function of temperature is relatively high compared to $2.2 \mu\text{m}$, is sensitive to different convection treatments which affect the temperature gradient in the interval $\tau_{\text{Ross}} = 1$ to ~ 3 . The model with the steepest gradient, PHOENIX “B” with $\alpha = 0.5$ and no overshooting, has the strongest limb darkening. ATLAS 12 model “E” with 100% overshooting has the shallowest gradient and the weakest limb darkening. ATLAS 12 model “F” and CO^5BOLD model “C1” have similar gradients and provide an intermediate degree of limb darkening which is consistent with the interferometric observations.

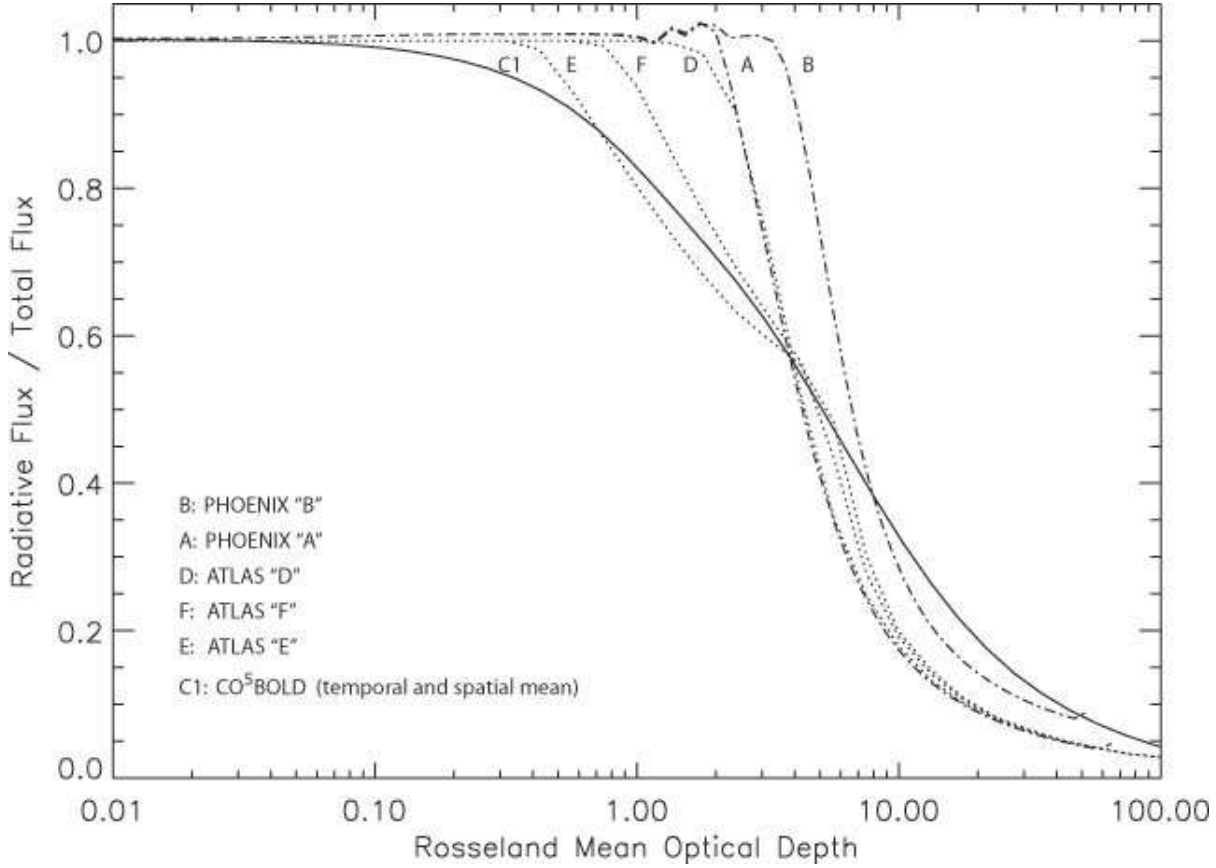


FIG. 8.— A comparison of the six model atmosphere radiative flux structures on a mean Rosseland optical depth scale: PHOENIX models “A” and “B” (dash-dot), ATLAS 12 models “D”, “E”, “F” (dot), and CO⁵BOLD model “C1” (solid). The 1-D overshooting models “E” and “F” and the temporally and spatially averaged 3-D model “C1” all have a significant fraction (5% to 15%) of their total flux in convection at an optical depth of unity, while the other 1-D models are fully radiative at this depth.